Highlights

On Extreme Waves in Directional Seas with Presence of Oblique Current

Jinghua Wang, Qingwei Ma, Shiqiang Yan

- The phase-resolved fully nonlinear numerical simulations of directional seas with presence of opposing and oblique current on large spatiotemporal scale are carried out.
- This study reports some new findings about how the fully nonlinear wave-current interactions modify the extreme wave properties in directional seas subject to current from different incident angles.
- The study also discusses whether the NewWave model is sufficient for describing the average shape of extreme waves induced by fully nonlinear wave-current interactions in directional seas.

On Extreme Waves in Directional Seas with Presence of Oblique Current

Jinghua Wang[a,b], Qingwei Ma[c,*], Shiqiang Yan[c]

[a]*School of Engineering, Ocean University of China, Qingdao, 266100, China*
[b]*Faculty of Engineering, National University of Singapore, 119077, Singapore*
[c]*School of Mathematics, Computer Science and Engineering, City University of London, London, EC1V 0HB, United Kingdom*

Abstract

This paper will address two questions: i) How the fully nonlinear wave-current interactions modify the extreme wave statistics, spectrum characteristics and average shape of extreme waves in directional seas with presence of current with different incident angles; ii) Whether the NewWave model is adequate to describe the average shape of nonlinear extreme waves in directional seas with presence of opposing and oblique current. This study employs fully nonlinear numerical simulations, and the results demonstrates that current can enhance the wave crest exceedance probability at distribution tail and kurtosis, broaden the spectra, and cause severe vertical and horizontal asymmetry of extreme wave profiles depending on the incident angle and initial steepness. The assessment on the NewWave models reveals that they fail to predict the reduction of the crest width with increasing current incident angle and significantly underestimate the asymmetry parameters for large steepness waves.

Keywords: Wave-current interactions, NewWave, Large-scale simulations, Phase-resolved wave modelling, Fully nonlinear potential model

1. Introduction

Extreme waves have been intensively studied in coastal and ocean engineering for decades. Their precise meaning is slightly different in different contexts.

*Corresponding author: q.ma@city.ac.uk

They are sometimes referred to the most probable maximum in a sea state (Tayfun and Fedele, 2007a), or sometimes to an exceptional large and high wave (i.e., rogue waves) (Pelinovsky et al., 2008), while in design practice they are referred to the maximum wave with a return period, e.g. 100 years (Tucker and Pitt, 2001). No matter what their special meaning is, their appearance is indicated by high kurtosis of free surface about mean water level and high tail values of wave crest exceedance probability distributions, and their kinematic and dynamic properties are reflected by their shapes and spectra. Therefore, many researchers have studied the kurtosis, crest exceedance probability, spectral properties and average shapes of extreme waves. Some studies were well documented in Dysthe et al. (2008), Kharif et al. (2009), Adcock and Taylor (2014) and Fedele et al. (2016). The following will summarize some key findings relevant to the topic of this study, which are categorized as those with or without considering current in unidirectional and directional (or spreading) seas.

In unidirectional seas (long-crest waves) without considering current, random wave field can be regarded as a superposition of many sinusoidal wave components with constant amplitude by assuming the waves to be small and described by a linear wave theory. The surface elevation can be represented by a Gaussian distribution, and the wave height follows Rayleigh distribution, while the kurtosis equals to about 3 (Longuet-Higgins, 1963, 1980). In addition, the NewWave theory (also known as the Slepian model (Lindgren, 1970) or Quasi-Determinism (QD) theory of large crest (Boccotti, 1983, 1989)) indicates that the average shape of the extreme waves is proportional to the scaled auto-correlation function, and the theory has been widely adopted to fit extreme wave profiles observed in field measurements, or reproduce extreme waves in numerical simulations or laboratory (Tromans et al., 1991; Boccotti et al., 1993; Boccotti, 2000; Christou and Ewans, 2014). However, the limitations of linear wave theories have been pointed out in many studies, e.g., the Rayleigh distribution underestimates the probabilities of extreme waves (Slunyaev and Sergeeva, 2012; Nørgaard and Andersen, 2016), neither can the linear NewWave model well describe the average shape of extreme waves featuring a sharper crest and shallower trough (Walker et al., 2004). To overcome such limitations, the second-order theories are introduced leading to improved wave crest exceedance probability comparing to field observation (Longuet-Higgins, 1963; Tayfun, 1980; Tayfun and Lo, 1990; Forristall, 2000). Besides, a second-order corrected NewWave profile was able to provide a reasonable approximation to the average extreme wave profiles as observed from field data (Whittaker et al., 2016; McAllister, 2017), though it is arguable that the apparent asymmetry of the recorded profiles in the field might indicate that the groups were not at the focusing point (Benetazzo et al., 2017). Nevertheless, the second-order theories underestimate the probability of extreme waves of heights greater than twice the significant height (which is now widely accepted as the criterion of rogue waves) and the kurtosis when wave steepness is large according to results collected from field and laboratory (Skourup et al., 1997; Onorato et al., 2004, 2006; Baschek and Imai, 2011). Later, the third-order Tayfun distribution considering the Stokes bound contribution for narrowband waves (Tayfun and Fedele, 2007b) was suggested to describe the wave height exceedance probability, which was shown in good agreement with the field observation (Fedele et al., 2016). Besides, the third-order effects on kurtosis for narrowband waves is investigated theoretically (Janssen, 2003, 2009; Onorato et al., 2008; Fedele, 2015), and the link between kurtosis and extreme wave probability was established while the wave height exceedance probability in terms of the third-order kurtosis was shown in good agreement with experiments for cases of kurtosis up to 3.62 (Mori and Janssen, 2006). Moreover, in contrast to the stationary spectrum described by the linear and second-order theories, the widening of the spectral bandwidth and downshift of the spectral peak was also pointed out in Janssen (2009)'s theoretical study and observed in the numerical simulation by using the modified nonlinear Schrödinger equation (MNLSE) that considered fourth-order wave nonlinearities (Dysthe et al., 2003), as well as in laboratory experiments (Slunyaev and Sergeeva, 2012). It also shows that the MNLSE produces improved estimation of the kurtosis than the second-order theories (Zhang et al., 2016). However, it was pointed out the results obtained by using MNLSE underestimated the exceedance probability of extreme waves, kurtosis and broadening of the spectral bandwidth through comparing with experiment results for modelling random waves based on a Gaussian spectrum (Slunyaev and Sergeeva, 2012). On the contrary, for a more general case based on JONSWAP spectrum, the MNLSE was shown to overestimate the kurtosis and probability of extreme waves (Toffoli et al., 2010; El Koussaifi et al., 2018). Nevertheless, the fully nonlinear approach can lead to improved results despite overestimating the statistics (Toffoli et al., 2010; Zhang et al., 2016). This is due to the narrow-bandwidth and small steepness assumptions adopted by the Schrödinger-type equations may not always be true (Xiao et al., 2013) and it becomes less accurate when spectral bandwidth and wave steepness are large (Wang et al., 2017). In addition, the NewWave model considering fifth-order Stokes-type corrections may be able to reproduce the New Year Wave reasonably well close to the peak with slightly overestimating the depth of the troughs (Walker et al., 2004). Though the adequacy of the NewWave model to represent the shape of large steepness waves has been demonstrated in many studies and properly accounting for nonlinear effects improves on the prediction (Jensen, 2005; Tayfun and Fedele, 2007a,b; Fedele and Tayfun, 2009; Alkhalidi and Tayfun, 2013), it cannot explain the group asymmetry, i.e., the so-called 'wall of water' or 'hole in the ocean'-like wave profile as observed in the ocean, laboratory and fully nonlinear numerical simulations (Gibbs and Taylor, 2005; Lindgren, 2006; Adcock et al., 2015; Cattrell et al., 2018; Tang et al., 2019).

In directional seas (short-crest waves) without considering current, the studies based on experiments in laboratory and weakly/fully nonlinear numerical simulations systematically investigated the effects of directionality on extreme wave statistics (Onorato et al., 2009; Waseda et al., 2009; Toffoli et al., 2010). They suggest that the changes in extreme wave probability, kurtosis, broadening spectral bandwidth and downshifting of the spectral peak with spreading angle less than 12^o basically agree with the findings for unidirectional seas according to the fully nonlinear numerical simulation results (Xiao et al., 2013; Slunyaev and Kokorina, 2020). However, the increase of spreading angles can lead to a significant reduction of extreme wave probability and kurtosis as confirmed in theoretical studies (Janssen and Bidlot, 2009; Fedele, 2015), numerical simulations by using the MNLSE (Socquet-Juglard et al., 2005) and fully nonlinear models (Bateman et al., 2001; Xiao et al., 2013). Thus, the second-order theory is sufficient to accurately predict the kurtosis and wave crest exceedance probability in directional seas (Fedele et al., 2016). This is due to the fact that the directionality can result in a transition to a weak non-Gaussian state, despite that the modulational instability still persists, albeit weak (Fadaeiazar et al., 2018, 2020). Besides, the NewWave model incorporating the directional spreading and a second-order Stokes-type correction can successfully describe the contraction of the crestedness of the extreme wave profile, which well agreed with field measurement (Jonathan and Taylor, 1997; Fedele et al., 2016; Benetazzo et al., 2017). Nevertheless, it was reported that the probability of gathering extreme waves within an in-situ space-time wave field is at least one order of magnitude higher than that obtained by restricting the analysis to time only (Benetazzo et al., 2017), implying that the second-order theory may underestimate the probability of extreme waves in space-time wave field. In addition, the broadening of spectrum were observed in the numerical simulation by using the MNLSE (Socquet-Juglard et al., 2005) and fully nonlinear model (Xiao et al., 2013), whereas the former overpredicts the spectral bandwidth especially for initially broader spreading cases (Xiao et al., 2013).

On the other hand, it has been widely recognized that the superposition of waves and current can provoke extreme waves (Lavrenov, 1998; White and Fornberg, 1998; Lavrenov and Porubov, 2006; Cattrell et al., 2018). Many studies have focused on unidirectional waves interaction with current and indicated that (i) wave height amplification around a caustic is caused by refraction (White and Fornberg, 1998; Janssen and Herbers, 2009) and enhanced by nonlinear wave-current interactions (Moreira and Peregrine, 2012), and (ii) wave-current interaction may induce modulational instability (Bakhanov et al., 1996; Stocker and Peregrine, 1999; Nwogu, 2009; Toffoli et al., 2011; Ruban, 2012; Ma et al., 2013; Manolidis et al., 2019). The latter is also associated with vertically shearing current (Choi, 2009; Thomas et al., 2012; Touboul and Kharif, 2016; Guyenne, 2017; Kharif et al., 2017; Liao et al., 2017). It has been found that the Rayleigh distribution significantly underestimates the extreme wave probability with presence of opposing current by the numerical simulations using a Schrödinger-type equation (Onorato et al., 2011) and by laboratory tests (Toffoli et al., 2015). Specifically, an opposing current yields the maximum extreme wave probability of one order greater than that based on the Rayleigh distribution and the maximum kurtosis larger than 4.5 (Toffoli et al., 2015). The deviation from the Gaussian state can be explained based on the current-modified NLSE, which shows that the coefficient of nonlinear term increases as the waves enter the current region. As a result, the increasing nonlinearities can excite the modulation instability that destabilizes the wave packet, and the concurrent intensification of the maximum wave growth depends on the ratio of current velocity over wave group speed (Onorato et al., 2011; Toffoli et al., 2013). Meanwhile, to describe the average shape of extreme waves, the NewWave theory incorporating uniform current is proposed, which suggests that an opposite current can enhance the significant height and peak frequency, and the enhancement is more remarkable if the velocity becomes greater (Arena et al., 2005).The second-order Stokes contribution is subsequently introduced to the NewWave model with superimposed current (QD theory of large crest-to-trough height to be precise), and it is found that the waves becomes higher in crest and flatter in trough than in absence of current (Nava et al., 2006). However, a forward tilting extreme wave front due to nonlinearities characterized by group asymmetry are observed in laboratory, which cannot be described by using the linear or second-order NewWave theories (Wu and Yao, 2004; Ma et al., 2013).

Some studies have also been carried out on interaction between directional waves and opposing (or adverse) current. Janssen and Herbers (2009) investigated the evolution of spreading waves over an opposing shearing current by employing a frequency-angular spectrum model accounting for cubic nonlinear dynamics and indicated that directionally spread wave fields generally maintained near-Gaussian statistics but behaved locally with strongly non-Gaussian statistics. The laboratory results (Toffoli et al., 2015) revealed that the maximum kurtosis of spreading wave fields subjected to opposing current can reach 3.5, higher than the linear value but lower than that of unidirectional wave fields subjected to opposing current. The publication also revealed that the presence of an opposing current made large waves occur more often and lifted the tail of the distribution, even with relatively weak current (0.15 times wave-group velocity). However, the study on spreading wave fields propagating over an oblique current is rare. More recently, a third-order nonlinear probability distribution model accounting for the space-time drifting effects is proposed and results showed that larger drift speed yields larger probability of encountering extreme waves compared with anchored vessel, while the probability increases in proportion to the drifting time (Fedele et al., 2017). Toffoli et al. (2011) carried out laboratory tests on the cases for current crossing the main direction of waves at the incident angles of 110° and 120°. They found that when the directional spreading broadens, the kurtosis preserves slightly higher values than that without current and can achieve a maximum increment by 15% compared to the cases without current. Nevertheless, relevant study on extreme waves induced by current from various incident angles in directional seas using fully nonlinear numerical models has not been carried out so far. Moreover, the average shape of extreme waves in directional seas with presence of current has not been investigated.

The studies above have made important contributions to perceiving the extreme wave properties. Nevertheless, the following two issues are still remaining unaddressed. Firstly, how does the nonlinear wave-current interactions modify the extreme wave statistics, spectrum characteristics and average shape of extreme waves in directional seas with presence of current at a range of incident angles? Secondly, whether can the NewWave model be employed to describe the average shape of extreme waves in directional seas with presence of opposing and oblique current, in particular for strong nonlinear cases? As aforementioned, the numerical model based on fully nonlinear potential theory can provide reliable statistical and deterministic descriptions about the extreme waves. Therefore, this study will aim to answer the two questions by using results derived from phase-resolved numerical simulations of directional random seas in presence of current at different incident angles and initial wave steepness based on the fully nonlinear ESBI model (Wang et al., 2018). Besides, the results from the model will also be used as benchmarks for verification against the NewWave models in order to examine their accuracy.

The paper is organized in the following way. Firstly, the formulations regarding different methodologies employed in this study are introduced in Section 2, i.e., the current-modified NewWave model based on linear theory, the nonlinear NewWave model considering the Stokes-type corrections and the ESBI model based on fully nonlinear potential flow theory. Section 3 presents the theoretical and numerical results for the cases with different incident angles between waves and current and discusses the current effects on the crest exceedance probability, kurtosis, spectral properties and average shapes of extreme waves. Moreover, the suitability of the NewWave model for describing the average shape of extreme waves in directional seas subject to current will be discussed both qualitatively and quantitatively in Section 4. Lastly, concluding remarks are given in Section 5. This study will contribute to an insight of the statistical properties of extreme waves induced by fully nonlinear wave-current interactions in directional seas subject to current with different incident angles and shed light on the fact that the NewWave model does not adequately describe the shape, and so the kinematics, of extreme waves when there exists strong interaction of spreading waves with current.

2. Methodologies

In this section, descriptions will be given on all the models that are used for studying the properties of extreme waves in directional seas with presence of current. These include the ones based on linear theory, second-order theory and fully nonlinear theory. Note that this study has assumed that the horizontal velocity of the current is independent of the vertical coordinate, which is a reasonable approximation to the current field in region where the characteristic time and length scale of the oceanic current is large compared with wind-generated waves (Peregrine, 1976). Nevertheless, the variation of its vertical structure can become important when considering wind driven surface current (Nwogu, 2009), which however is not the focus of this study.

2.1. Current-modified NewWave model based on linear theory

The NewWave model describes the average shape of the extreme waves with the given spectrum of sea states. It should be noted that the NewWave theory can be employed to either examine the average shape of extreme waves in time domain at specified location using the time histories of free surface elevation or frequency spectrum (Boccotti, 2000), or investigate their average shape in space domain based on the wavenumber spectrum (Gibbs and Taylor, 2005). This study will adopt the latter to explore the average shape of extremes in space subject to opposed or oblique current. In other words, with the wave spectrum known in advance, the free surface elevation of the averaged extreme wave profile can be obtained by (Gibbs and Taylor, 2005)

$$\eta_{NW}^{(0)}\left(\boldsymbol{x}\right) = \frac{a_0}{m_0} \int S_0\left(\boldsymbol{k}\right) \cos\left(\boldsymbol{k}\cdot\boldsymbol{x}\right) \mathrm{d}\boldsymbol{k} \tag{1}$$

where $\eta_{NW}^{(0)}$ denotes to the profile of the NewWave, a_0 is the desired crest height of the NewWave and m_0 is the zeroth moment of $S_0\left(\boldsymbol{k}\right)$, $S_0\left(\boldsymbol{k}\right)$ represents the corresponding wavenumber spectrum without effects of current, $\boldsymbol{x} = (x, y)$ and $\boldsymbol{k} = (k_x, k_y)$ are the horizontal spatial coordinates the wavenumber vectors, respectively. Following Boccotti (1989) and Arena et al. (2005), the NewWave profile with presence of current $\eta_{NW}^{(c)}$ can be expressed by

$$\eta_{NW}^{(c)}\left(\boldsymbol{x}\right) = \frac{a_c}{m_0^{(c)}} \int S\left(\boldsymbol{k}\right) \cos\left(\boldsymbol{k}\cdot\boldsymbol{x}\right) \mathrm{d}\boldsymbol{k} \tag{2}$$

where a_c is the desired crest height, $m_0^{(c)}$ is the zeroth moment of $S\left(\boldsymbol{k}\right)$ and $S\left(\boldsymbol{k}\right)$ is the spectrum considering current effects. Now the problem is reduced as how to determine $S\left(\boldsymbol{k}\right)$. For this purpose, we follow the suggestion for general wave spectra of directional waves in presence of current by Lavrenov (1998, 2003), i.e.,

$$\hat{S}\left(\omega, \theta\right) = \frac{16\hat{S}_0\left(\omega, \theta_0\right)}{\sqrt{1 + u'\cos\left(\varphi - \theta\right)}\left[1 + \sqrt{1 + u'\cos\left(\varphi - \theta\right)}\right]^4} \tag{3}$$

where $\hat{S}_0(\omega, \theta_0)$ and $\hat{S}(\omega, \theta)$ represent the directional spectra without and with current, respectively, θ_0 and θ denote the direction of wave propagation before and after encountering the current as shown in figure 1. In equation (3), $u^{'} = 4\omega u/g$ where $u = |\boldsymbol{u}|$ is the magnitude of the current speed, g is the gravitational acceleration, and ω is the frequency measured in an immovable coordinate system, which can be different from the frequency σ measured in the moving frame with the current. The two frequencies are connected through

$$\omega = \sigma + \boldsymbol{u} \cdot \boldsymbol{k} \tag{4}$$

where $\boldsymbol{u} = (u \cos\varphi, u \sin\varphi)$ and φ is the incident angle of the current.

To make use of equations (3) and (4) for approximating the NewWave profile, the wavenumber spectrum $S(\boldsymbol{k})$ can be derived from the directional spectrum $\hat{S}_0(\omega, \theta_0)$ and by $\hat{S}(\omega, \theta)$ using the following transformation (Tucker and Pitt, 2001)

$$S_0(\boldsymbol{k}) = \hat{S}_0(\omega, \theta_0) \frac{\partial(\omega, \theta_0)}{\partial(k_x, k_y)} = \hat{S}_0(\omega, \theta_0) \frac{g}{2\omega k} \tag{5}$$

$$S(\boldsymbol{k}) = \hat{S}(\omega, \theta) \frac{\partial(\omega, \theta)}{\partial(k_x, k_y)} = \hat{S}(\omega, \theta) \left(k \frac{\partial k}{\partial \omega}\right)^{-1} \tag{6}$$

Note that equation (3) can be further written as a formulation in terms of the wave amplitude, which then becomes the one suggested by Nwogu (1993). As well-known, one can express $\hat{S}_0(\omega, \theta_0)$ as $\hat{S}_0(\omega, \theta_0) = \hat{S}(\omega) G(\theta_0)$ with the spreading function $G(\theta_0)$ given by

$$G(\theta) = \frac{\Gamma(N/2 + 1)}{\sqrt{\pi}\Gamma[(N+1)/2]} \cos^N(\theta) \tag{7}$$

where $\hat{S}(\omega)$ is the spectrum for unidirectional waves (note that the frequency-dependent spreading function can be selected for a more realistic simulation). For unidirectional irregular waves, integrating equation (3) with respect to θ gives the expression obtained by Huang et al. (1972), while the current-modified NewWave model of equation (2) reduces to the version for long-crested waves (Arena et al., 2005). Further replacing $\hat{S}(\omega)$ with the wave amplitude, one obtains the well-known relationship of wave amplitude and current suggested by Longuet-Higgins and Stewart (1961). Readers may refer

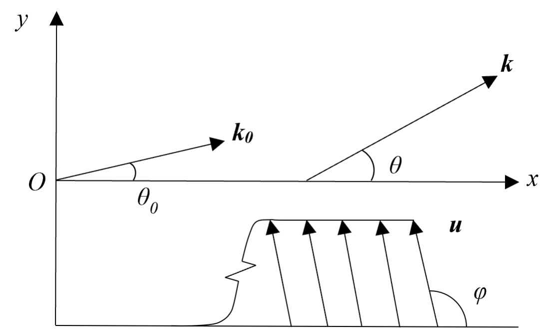

Figure 1: Sketch of the problem in plan view.

to Appendix A and the aforementioned literature for more details about deriving the formulations of the current-modified NewWave model.

In this study, the directional spectrum before interacting with current and the spatial distribution of the current velocity field are specified. Thus, the average shape ($\eta_{NW}^{(c)}$) of extreme waves in presence of current, based on the linear theory, can be estimated by employing equations (2)∼(6).

2.2. Current-modified NewWave models considering nonlinear effects

In addition to the model established above using the linear theory, two other models through involving nonlinear effects are formulated. The first one is to employ the directional spectrum in presence of current collected from the fully nonlinear numerical simulations (to be discussed in the next subsection) and then to use equation (2) to directly convert the spectrum into the average shape of extreme waves. In this method, the average shape contains both nonlinear and current effects through the wave spectrum but is still based on linear relationship of equation (2). The results obtained by this method will be denoted as $\eta_{NW}^{(c1)}$ hereafter.

Alternatively, the NewWave profile with some nonlinear effects may be formed through the Stokes-type correction up to the second order as suggested by Walker et al. (2004), which is expressed as

$$\eta_{NW}^{(c2)} = \eta_L + \eta_2 + O\left(\varepsilon^3\right) \tag{8}$$

where η_L is the linear part that can be replaced with $\eta_L = \eta_{NW}^{(c)}$ in section 2.1, η_2 is the second-order correction term and can be estimated by using the formula

$$\eta_2 = \frac{k_p}{2}\left(\eta_L^2 - \eta_{LH}^2\right) \tag{9}$$

where η_{LH} is the Hilbert transform of η_L and k_p the peak wavenumber. Note that an alternative approach is to use the MNLSE formulation or the exact second-order interaction kernal that calculates the wave-wave interaction components for all possible pairs of linear wave components as demonstrated in Jensen (2005) and Tayfun and Fedele (2007a) in absence of current and in Nava et al. (2006) with presence of current. However, it has been pointed out that the estimation based on equation (9) agree very well with those by using the exact second-order theory (Dean and Sharma, 1981; Dalzell, 1999) for describing the profiles of New Year Wave in directional seas without presence of current (Walker et al., 2004). Therefore, the robustness of equation (9) should be sufficient for investigating the second-order nonlinear effects on the average shape of extreme waves in directional seas in presence of current. Note that although Stokes-type correction leads to a better description for sharper crest and shallower trough, a drawback is that it produces a symmetrical wave profile (Lindgren, 2006), which will be addressed later in this study.

On the other hand, for the strongest nonlinear case considered in this study (as later show in Section 3 with largest initial wave steepness and 180^o opposed current), it is found that the magnitude of the nonlinear contributions decreases rapidly as the order increases. For instance, the maximum contribution of the third-order correction to the peak of NewWave profile is about 3.7%. Heuristically, for other cases in this study, the resulted contributions from the third-order correction part will be less than this case. Therefore, the nonlinear NewWave model considering the Stoke-type corrections up to the second-order is employed, which is sufficient regarding the purpose of this study. Therefore, if the NewWave model with the nonlinear correction described in this section still cannot well model the extreme waves, its deficiency may be due to the lack of considering nonlinearities beyond the Stokes-type corrections (Lindgren, 2006).

2.3. Method for fully nonlinear simulations

In this study, the Enhanced Spectral Boundary Integral (ESBI) method for modelling fully nonlinear wave-current interactions (Wang and Ma, 2015; Wang et al., 2018) is employed to simulate directional waves subject to current with different incident angles. The details of the method are well documented in Wang and Ma (2015) and Wang et al. (2018). Only some key equations are briefed here for completeness.

All the variables used in the ESBI have been non-dimensionalized, e.g., those in length are multiplied by peak wavenumber k_p, i.e., $(\boldsymbol{X}, Z) = k_p(\boldsymbol{x}, z)$, those in time by peak wave frequency ω_p, i.e., $T = \omega_p t$, velocity potential by k_p^2/ω_p and velocity by k_p/ω_p, and the dispersion relation is given by $\omega_p = \sqrt{gk_p}$. The still water level is specified at $Z = 0$, while the free surface and velocity of the water can be split into two parts, i.e.,

$$\zeta = \overline{\eta} + \eta \tag{10}$$

$$\overrightarrow{U} = \overrightarrow{U} + (\nabla, \partial_Z)\,\phi \tag{11}$$

where $\nabla = (\partial_X, \partial_Y)$ is the horizontal gradient operator, $\overrightarrow{U} = (\boldsymbol{U}, W)$ and $\overline{\eta}$ are the current velocity and current induced surface elevation in absence of waves, respectively; ϕ and η are the velocity potential and deflection of the free surface involving the contribution from waves and wave-current interactions. Then the free surface boundary conditions based on the fully nonlinear potential theory can be reformulated as

$$\partial_T \overrightarrow{M} + A\overrightarrow{M} = \overrightarrow{N} \tag{12}$$

where

$$\overrightarrow{M} = \begin{pmatrix} KF\{\eta\} \\ K^{3/2}F\{\widetilde{\phi}\} \end{pmatrix}, A = \begin{bmatrix} 0 & -K^{1/2} \\ K^{1/2} & 0 \end{bmatrix} \text{ and } \overrightarrow{N} = \begin{pmatrix} KF\{G_1\} \\ K^{3/2}F\{G_2\} \end{pmatrix}, \tag{13}$$

$\widetilde{\phi}$ denotes the values at the surface, $F\{*\} = \int * \mathrm{e}^{-\mathrm{i}\boldsymbol{K}\cdot\boldsymbol{X}}\mathrm{d}\boldsymbol{X}$ is the Fourier transform and $F^{-1}\{*\}$ denotes the inverse transform, the wavenumber $K = |\boldsymbol{K}|$, and formulations of G_1 and G_2 can be found in Appendix B. Equation (12) will be used as the prognostic equation for updating the free surface and velocity potential in time domain and its solution can be given by

$$\overrightarrow{M}(T) = e^{-A(T-T_0)}\left[\int_{T_0}^{T} e^{A(T-T_0)}\overrightarrow{N}\mathrm{d}T + \overrightarrow{M}(T_0)\right] \tag{14}$$

where

$$e^{A\Delta T} = \begin{bmatrix} \cos K^{1/2}\Delta T & -\sin K^{1/2}\Delta T \\ \sin K^{1/2}\Delta T & \cos K^{1/2}\Delta T \end{bmatrix}. \tag{15}$$

Equation (14) can be solved by using the fifth-order Runge-Kutta method with adaptive time step. An energy dissipation model suggested by Xiao et al. (2013) is also introduced to the ESBI to handle breaking waves, of which the efficiency has been demonstrated and confirmed by direct comparison against laboratory measurements.

To update the $\widetilde{\phi}$ and η in time domain, the vertical velocity V requires to be calculated each time step. The evaluation of V can be achieved by using the boundary integral equation, and it can be split into four parts in terms of different degrees of nonlinearities, i.e., $V = V_1 + V_2 + V_3 + V_4$, where the formulations for each part can be found in Appendix B. For more details about the numerical scheme, readers can refer to Wang et al. (2018).

Wang et al. (2018) carried out necessary verification by comparing results from the above method with analytical solutions, and also validation by comparing with experimental data in several cases that include two-dimensional focusing waves on a uniform current, two-dimensional regular waves interacting with spatially-varying current and three-dimensional interactions of horizontally varying current with spreading ocean waves and modulated waves generated by superimposing two-sideband wave components onto a carrier wave component. Their studies showed that the numerical results from the method are almost the same as the analytical solutions when the wave steepness is sufficient small, and in particular, showed that their numerical results agree quite well with experimental data in all the cases they studied. On the basis, this paper will not present results related to the validation on the numerical method, rather focus on discussing the outcome of modelling extreme waves in directional seas interacting with opposing and oblique current. Readers can refer to Wang et al. (2018) for the results of validations.

3. Results and discussion

3.1. Wave condition, current field and numerical setups

For the purpose of this paper, the cases with different parameters of wave and current are studied. Specifically, the waves are generated by using the JONSWAP spectrum and spreading function of equation (7) with $\gamma = 9$, peak frequency $\omega_p = 1.17 rad/s$ (a peak wave length, L_p, of about 45m), and

$N = 24$. Two values of wave steepness for the spectrum are specified, i.e., $(k_pH_s)_0$= 0.01 and 0.15; hereafter they are called initial steepness. The usage of JONSWAP spectrum with $\gamma = 9$ is a good approximation of a swell spectrum restricted to a narrow bandwidth (Goda, 1983), while the selected large wave steepness $(k_pH_s)_0$= 0.15 is not unusual as similar values were observed during ship accidents due to bad weather conditions (Toffoli et al., 2005). The selected bandwidth parameter and steepness yields a BFI of 0.16, which is similar to the sea state where the Killard wave is observed (Fedele et al., 2016). To consider relatively smaller BFIs, two steepness $(k_pH_s)_0$= 0.05 and 0.1 are also used for simulating the cases with a fixed current incident angle of 150°. In numerical simulations, the spectrum is cut-off at $1.55\omega_p$, corresponding to 1% of the spectral peak value. Computational setup is sketched in figure 2. Although the spectral components with frequency higher than $1.55\omega_p$ are ignored for wave generation, the components with higher frequencies will be produced leading to a broader-band spectrum (with $\gamma < 9$) during the fully nonlinear simulations in the area away from the wave generation zone due to fully nonlinear wave-wave and wave-current interactions, which is also known as weak wave turbulence (Fadaeiazar et al., 2018, 2020).

The current is specified according to the equation below

$$|\boldsymbol{U}| = \begin{cases} 0, & X/L_p \leq 2 \\ U_m H\left(\left(4 - X/L_p\right)/2\right), & 2 < X/L_p \leq 4 \\ U_m, & X/L_p > 4 \end{cases} \tag{16}$$

as shown in figure 2. To explore the effects of different current incident angles, a series of angles ranging from $\varphi = 90°$, 110°, 135°, 150° and 180° are selected whereas the current magnitude is fixed to $U_m = 0.3\ c_g$, where c_g is the wave group velocity. The selection of the wave parameters and current magnitude is consistent with the representative wave and current condition for studying current induced extreme waves in Agulhas region (Lavrenov, 1998), and other areas globally, e.g., South China Sea (Fang et al., 1998; Li et al., 2016).

The computational domain is selected to be $50L_p \times 50L_p$ as shown in figure 2, and is resolved into 2048×1024 collocation points in X- and Y-direction, respectively, where L_p is the non-dimensionalized peak wavelength without current in presence. Based on the relevant studies by Wang et al. (2018), the size of the domain is large enough for the wave-current interaction to become established and the resolution is fine enough for the results to converge. Pneumatic directional wavemaker (Clamond et al., 2005) is in-

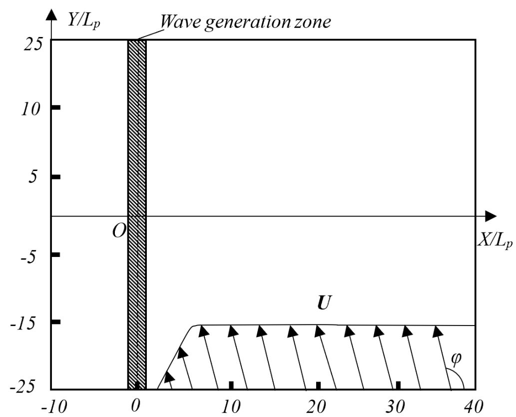

Figure 2: Plan view of the computational domain used in the simulations.

stalled along the Y-direction with $10L_p$ away from the left boundary and the domain in the region of $40L_p \times 50L_p$ on the right-hand side is used for effective wave field. The pneumatic wavemaker is implemented by prescribing a dynamic pressure distribution at the surface that is localized in space (as indicated by the shaded strip in Figure 2) and oscillates in time based on a linear wave generation theory. The waves excited by the oscillating pressure will then propagate towards the far field and nonlinear components will be generated through wave-wave interactions immediately after the waves moving away from the wavemaker (Clamond et al., 2005). Absorbing boundaries are employed to damp outgoing waves. To explore the extreme wave (defined in time domain) statistics, the surface time histories are collected by gauges deployed every $3L_p$ and $3.5L_p$ in X- and Y-direction, respectively, which is $12\times11 = 132$ in total number. This will avoid the issue that using a single point observation is insufficient to investigate the extreme wave ensembles (Benetazzo et al., 2017). Regarding the average shape of extreme waves, they are defined in space domain and more details are reported in section 3.4.

For each case with a given initial wave steepness $(k_pH_s)_0$ and current incident angle φ, four realizations are performed with different sequences of random numbers used in computing the phases of wave components. Note that the random phase approach is employed, which is equivalent to the random amplitude approach for generating random waves as sufficient number of components ($\approx 2\times10^3$) have been used in the numerical simulations (Tucker et al., 1984). Each simulation lasts for 500 peak periods to represent a typical sea state. The first 100 peak periods are used for waves ramp-up to ensure all the interesting spectral components to interact with the current and reach the absorbing boundary at the other end. Therefore, the free surface records from 100∼500 periods are used for analysis, which means that about 5×10^4 waves are collected from the probes in each simulation and it is sufficient for achieving reliable statistical analysis (Toffoli et al., 2011) and building up the nonlinear spectra to steady state (Nwogu, 1993). For example, the error of estimated kurtosis reduces in time and becomes less than 5% after 400 periods, indicating that the selected time range is sufficient for achieving stabilized statistics. In addition, the free surface spatial distribution at every peak period is saved to files for estimating the wavenumber spectra and average shape of extreme waves. Some snapshots of the non-dimensional free surface elevation η at the end of the simulations are displayed in figure 3(b-d) for the case with $(k_pH_s)_0 = 0.15$ and different current incident angles. Figure 3(a) gives corresponding results without current. It can be seen from this figure that the number of large waves for the cases with current is significantly larger than the cases without current, implying that the presence of the current has direct impacts on the surface deflection in directional seas, as well as the appearance of extreme wave events. Further discussions will be presented in the following subsections.

3.2. Current effects on exceedance probability and kurtosis

Firstly, the effects of wave-current interactions on the two aspects of extreme wave statistics will be investigated. One is the wave crest exceedance probability and the other is the kurtosis. Both are used by many researchers as statistical indicators of the extreme waves. The discussions will be based on the results of free surface time sequence collected from the wave gauges deployed in the numerical simulations by the ESBI method.

3.2.1. Wave crest exceedance probability

For a Gaussian sea, the exceedance probability of wave crest can be represented by the Rayleigh distribution, given by Kharif et al. (2009)

$$P_R = \exp\left(-8\chi^2\right) \tag{17}$$

where $\chi = H_c/H_s$ and H_c is the crest height (vertical distance from mean water level to crest peak, different from the wave height defined above). Equation (17) is only accurate for describing the statistics for small steepness waves where the second-and higher-order nonlinear effects are insignificant.

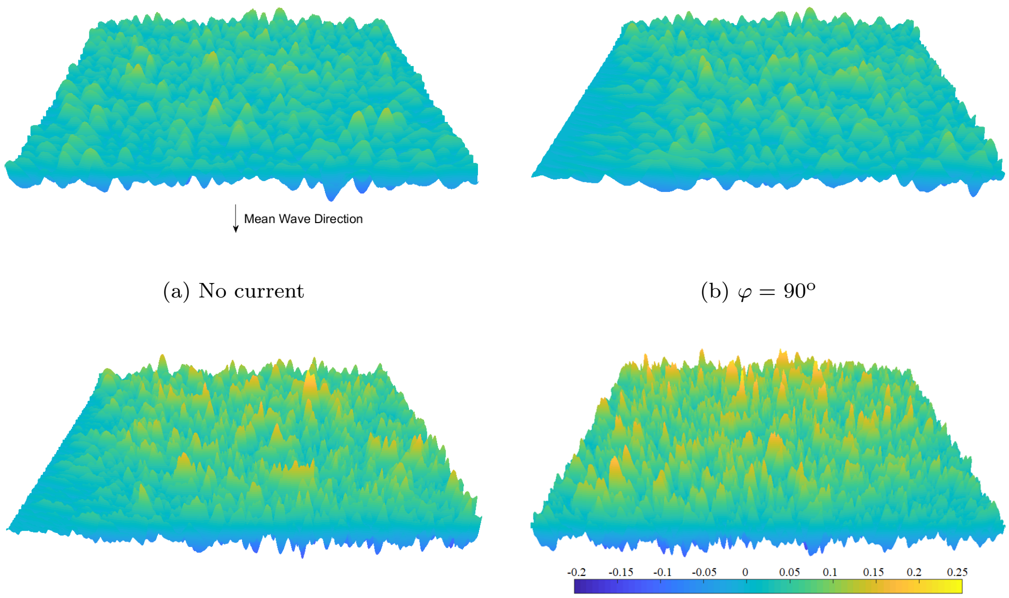

(a) No current

(b) $\varphi = 90^o$

(c) $\varphi = 135^o$

(d) $\varphi = 180^o$

Figure 3: Selected free surface snapshot at the end of simulation for $(k_p H_s)_0 = 0.15$.

To consider nonlinear effects, the Tayfun distribution was suggested, which describes the contribution from the nonlinearities up to the second-order for narrow-band nonlinear ocean waves (Tayfun, 1980). It is found that the prediction by Tayfun distribution agrees very well with both the real-world measurement and fully nonlinear numerical simulation by using HOS method without presence of the current (Fedele et al., 2016). Its mathematical form is given as

$$P_T = \exp\left[-\frac{\left(-1+\sqrt{8\sigma\chi+1}\right)^2}{2\sigma^2}\right] \tag{18}$$

where σ is 1/3 of the skewness of the free surface elevation. Note that the third-order Tayfun distribution becomes dependent on the excess kurtosis (Tayfun and Fedele, 2007b), which requires an accurate estimation of the kurtosis in *priori*. A detailed investigation of the kurtosis will be carried out in the subsequent section, therefore it is not employed here. Note that Fedele et al. (2017) has suggested a methodology to approximate the drifted spectral moments for estimating the nonlinear space-time statistics. Instead, we employ the surface elevation time histories collected from the probes deployed in the fully nonlinear simulations to estimate the spectral moments, which already considered the current effects. The exceedance probabilities of wave crests according to wave elevation obtained by the fully nonlinear numerical simulations based on ESBI method are presented in figure 4 for different current incident angle and wave steepness, together with the prediction from equations (17) and (18). The figure shows that the exceedance probability for the small steepness waves by the numerical simulations agrees generally well with the Rayleigh distribution for the cases with and without the current (except the case $\varphi = 180^o$ where the measured probability is slightly higher than the theoretical prediction at the tail). However, for larger steepness waves, the Rayleigh distribution leads to a significant underestimation of fully nonlinear results. In contrast, the Tayfun distribution successfully predicts the wave crest exceedance probability for the case with larger steepness and without the current, as shown in figure 4(a). However, the Tayfun model significantly underestimates the exceedance probability of nonlinear waves interacting with current, interestingly even when the incident angle is 90^o. For the case of 90^o incident angle, the current is only normal to the main direction waves but not to other wave components in directional seas. Thus, it is reasonable to see the difference in figure 4(b).

To examine the effects of current incident angle on the wave crest exceedance probability, the results obtained from the numerical simulations are displayed in figure 5. In figure 5(a), it can be found that the curves representing the exceedance probability of the cases with small wave steepness with different current incident angles match with each other very well, which again confirms the validity of the Rayleigh distribution for modelling the wave crest exceedance probability for small steepness waves, no matter the current is in presence or not. On the contrary, figure 5(b) depicts a totally different scenario for the cases with larger wave steepness, where it is found the presence of the current enlarges the wave crest exceedance probability for $H_c/H_s > 0.6$, indicating higher probability of extreme wave occurrence than the situation without current. When the current incident angle increases from $\varphi = 90^o$ to $\varphi = 135^o$, the exceedance probability gradually grows in magnitude. However, when the current incident angle is larger than 135^o, the exceedance probability does not significantly grow anymore, though slightly drops in the range H_c/H_s >1.2. The reduction of the probability in range H_c/H_s >1.2 for the cases $\varphi = 150^o$ and 180^o is because that the maximum wave crest heights are limited due to wave breaking, as indicated by the Type 4 probability distribution (Adcock and Taylor, 2014). It is noted that Toffoli et al. (2015) presented the wave height (not crest height) probability in directional seas subjected to opposing current and indicated the similar phenomenon that the current can lift the tail of the distribution. However, their results did not show such big difference as observed in figure 4(f) and figure 5(b). We simulated their cases and analyzed the wave height probability in the same way as they did and found that our numerical results are very close to theirs. As these results just confirm those in the reference and do not add any new thing, they are not presented here.

In summary, the presence of current will significantly enhance the wave crest exceedance probability for the cases with strong nonlinear interaction between waves and current. The extent of enhancement depending on the incident angle of current. The maximum enhancement occurs at the incident angle of 135^o but not at 180^o, in the cases studied. Under the conditions, the Tayfun distribution gives better prediction than the Rayleigh distribution, but it still significantly underestimates the probability, particularly at its tail. The largest difference between Tayfun distribution and fully nonlinear results is observed also at the current incident angle of 135^o.

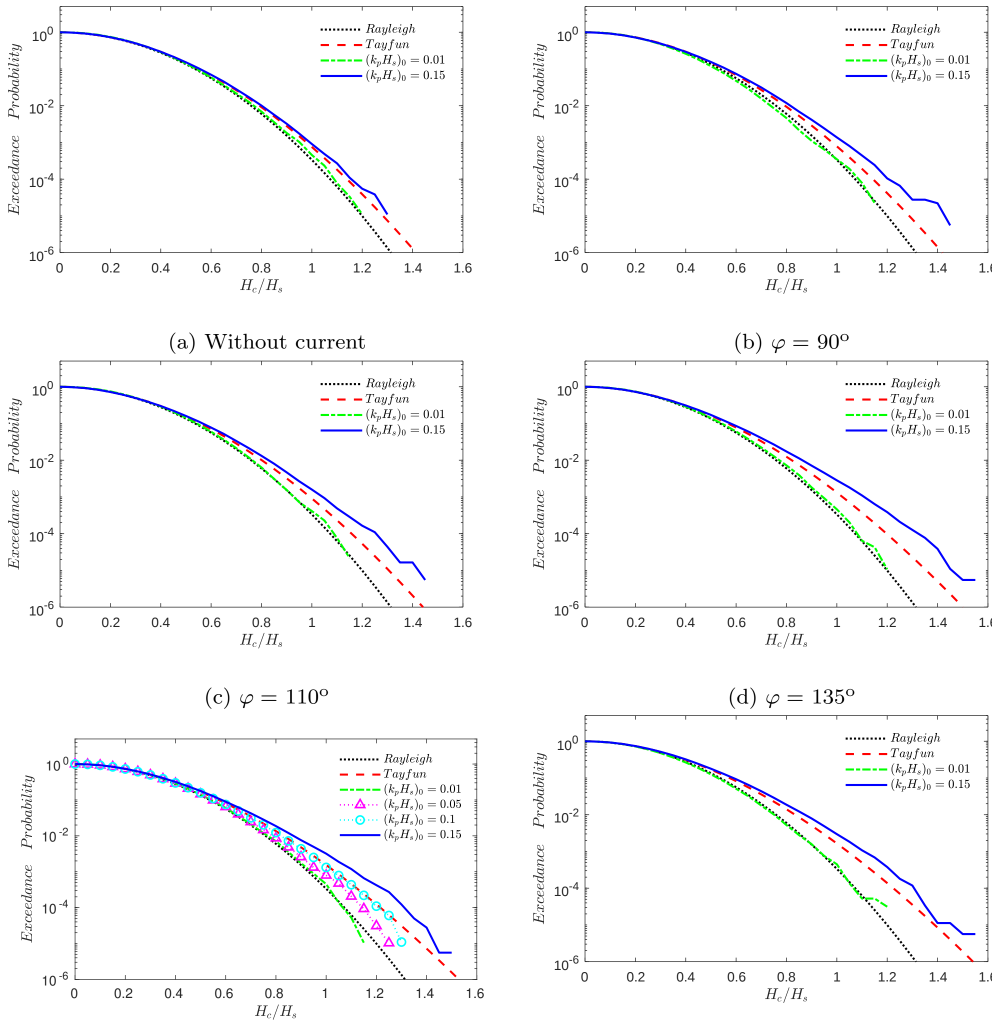

(a) Without current

(b) $\varphi = 90^o$

(c) $\varphi = 110^o$

(d) $\varphi = 135^o$

(e) $\varphi = 150^o$

(f) $\varphi = 180^o$

Figure 4: Exceedance probability of the wave crest in comparison with the Rayleigh and Tayfun distribution.

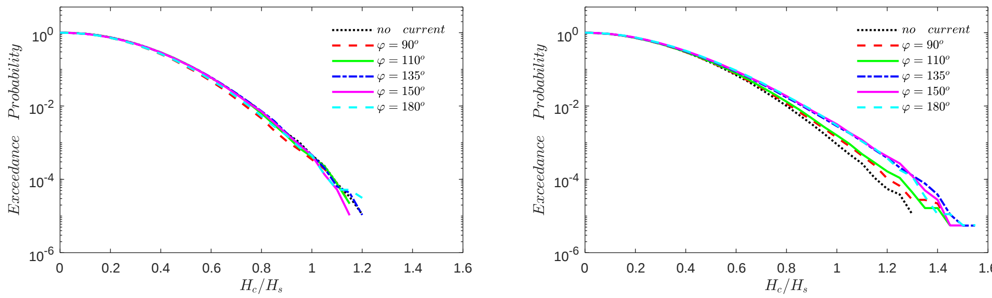

(a) $(k_pH_s)_0 = 0.01$

(b) $(k_pH_s)_0 = 0.15$

Figure 5: Exceedance probability of the wave crest for (a) small and (b) large steepness waves.

3.2.2. Kurtosis

Another effective way to investigate the probability of extreme waves is to examine the kurtosis of the surface elevation. The estimation of kurtosis depends on the wave theory assumed. When the wave steepness is small, it can be approximated by the linear theory, and thus the kurtosis is a constant, i.e., $\kappa_1 = 3$. For moderate waves, formulas were suggested to estimate the kurtosis to consider nonlinear effects up to the third order including a dynamic part and Stokes bound contribution, of which the former requires to estimate the wave steepness, spectral bandwidth and angular width in *priori* (Janssen and Bidlot, 2009; Fedele, 2015; Janssen and Janssen, 2019). In particular, the estimation of the width of observed frequency spectra is not a trivial task, while the usual approach will not always provide the sharpest estimate of directional width near the peak. Since discussion on the inefficacy of the approach for estimating kurtosis is not the focus of this study, for simplicity, the formula of kurtosis for a steady narrowband wave train considering third-order Stokes contribution is adopted (Mori and Janssen, 2006), i.e.,

$$\kappa_2 = 3 + 24k_p^2 m_0 \tag{19}$$

where m_0 is the total spectral energy. Thus, equation (19) allows the user to estimate the kurtosis for a given spectrum that, in presence of current, can be obtained by equations (3)$\sim$(6). For general nonlinear waves, one can adopt the formula

$$\kappa_3 = m_4/m_2^2 \tag{20}$$

to directly estimate the kurtosis, where m_2 and m_4 are the second and fourth moment of the surface elevation and obtained by integrating the wave time history, respectively, which are collected in the fully nonlinear numerical simulations. This way for estimating the kurtosis corresponds to the ensemble-averaged approach employed by Janssen (2003), where he had used time histories of surface elevation at arbitrary locations collected in a large number of Monte Carlo simulations by using the Zakharov equation.

The kurtosis estimated by using equation (20) based on the results of the fully nonlinear numerical simulation, together with the predictions based on the linear and the third-order theory, i.e., $\kappa_1 = 3$ and equation (19), are presented in figure 6. It can be observed in this figure that the linear prediction, and the kurtosis based on equations (19) and (20) with using the value of m_0 , m_2 and m_4 for the waves with smaller initial steepness agree generally well, which approximately equal to 3. In the cases with smaller steepness, the inclusion of current doesn't affect the magnitude of kurtosis. However, for the cases with larger wave steepness, the estimation of the kurtosis using equations (19) and (20) becomes much larger than 3 depending on the current incident angles. Equation (19) based on the third-order theory predicts that the current in perpendicular direction does not increase the kurtosis comparing with the case without current while the kurtosis from the equation grows with the increase of the current incident angle and becomes stabilized at around 3.08 when $\varphi \geq 150^{\text{o}}$. In contrast, the kurtosis given by equation (20) based on the results of fully nonlinear simulations is much larger compared with the third-order predictions in particular at the large incident angles. which is not surprising as equation (19) has not considered the dynamic part accounting for the nonlinear resonant interactions, which usually gives rise to a much larger contribution to the kurtosis (Mori and Janssen, 2006). Specifically, when there is no current, the estimated kurtosis based on equation (20) is slightly larger, which is due to nonlinearity of waves and is in line with those shown in figure 4(a) that the wave crest exceedance probability obtained by the numerical results is relatively larger than the Tayfun distribution based on the second-order theoretical prediction. For the cases with the incident angle of current from $\varphi = 90^{\text{o}}$ to $\varphi = 135^{\text{o}}$, the kurtosis estimated by equation (20) increases to the maximum value of 3.23 then reduces to 3.18 as the angle towards $\varphi = 180^{\text{o}}$. The observation of the reduction of the kurtosis for the two cases $\varphi = 150^{o}$ and 180^{o} are in consistence with the dropping of wave crest exceedance probability in the range $H_c/H_s > 1.2$ as depicted in figure 5(b). As restated, the up-limit of the wave height is bounded by the wave breaking for the cases of $\varphi = 150^{o}$ and 180^{o}, leading to the decrease of the kurtosis relative to the maximum value.

Overall, the deviations of wave crest exceedance probability at the distribution tail and kurtosis from the Gaussian sea for the larger steepness case basically corroborate that the current-induced increase of wave steepness triggers effects related to the modulational instability that compensates for the suppression of non-Gaussian behaviour due to large directional width (Toffoli et al., 2011). With increasing current incident angle, the component of the current speed in the mean wave direction becomes larger leading to further compression of the wavelength and enhancement of the wave steepness. As a consequence, the compensation effects become more significant so that these statistical properties exhibit more evident non-Gaussian behaviour. However, in contrast to Toffoli's speculation, stronger opposition or larger incident angle of ambient current does not necessarily produce higher kurtosis, e.g., $\varphi = 150^{o}$ and 180^{o}, which is attributed to that the enhancement of the wave steepness is bounded by the wave breaking. In addition, as shown in Figure 4(e) and Figure 6(b), given a fixed current incident angle, the increasing wave steepness can also enhance the crest exceedance probability and kurtosis. The larger the initial steepness is, more evident deviations are observed between the numerical results and the Gaussian sea. This is because larger steepness implying enhanced BFI will lead to stronger nonlinearities associated with modulational instability, which destabilizes the wave packet and facilitates the formation of extreme waves. Note that even cases of relatively small initial steepness $(k_pH_s)_0$=0.05 exhibit non-Gaussian sea behaviours. This is due to the enhancement to the wave steepness induced by current, which will be discussed in the next subsection.

3.3. Changes in wave spectral properties due to current

Next, it is important to look at the changes in the spectral properties due to wave-current interactions, as some fundamental features of the sea state, i.e., spectral shape, total energy and peak wavenumber, will be modified significantly due to the presence of current. We study the wavenumber spectra by their averaged shapes, which are estimated through performing Fourier transform to the free surface spatial distribution and calculating the mean

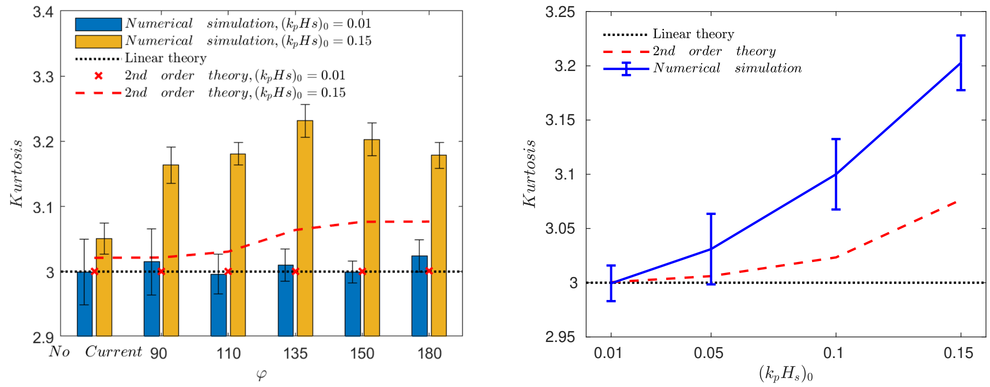

(a) (b)

Figure 6: Kurtosis versus (a) current incident angle and (b) wave steepness.

value within 100$\sim$ 500 peak periods for each case. The spectra of the first 100 periods are ignored so that only those of steady state are used for estimating the average shape. This has allowed sufficient time for the nonlinear wave-current interactions to reshape the spectra. For convenience, we use $\widetilde{S}_0\left(k\right)$ and $\widetilde{S}\left(k\right)$ to denote the estimated average spectral shape from numerical simulation results without and with presence of current, respectively.

3.3.1. Spectral shape and spreading

The spectra based on the linear theory model in equations (3)$\sim$(6), i.e. $S_0\left(\boldsymbol{k}\right)$ and $S\left(\boldsymbol{k}\right)$, and these based on the numerical simulation results, i.e., $\widetilde{S}_0\left(\boldsymbol{k}\right)$ and $\widetilde{S}\left(\boldsymbol{k}\right)$, corresponding to different current incident angles φ and initial wave steepness $(k_pH_s)_0$ for the cases without current or with current of $U_m/c_g \approx 0.3$ are displayed in figure 7. In the figure, the wavenumbers in both directions are normalized by the peak wavenumber. It is found that without current, the wavenumber spectra are symmetrical with respect to $k_y = 0$, as shown in figure 7(a), in which the contour of a spectrum with significant values is an ellipse with its major axis in k_y-direction. When the ambient current is $\varphi \geq 90^o$, the spectra are skewed in anti-clockwise direction around the peak wave number and becomes asymmetrical with respect to $k_y = 0$. This is because the wave components of $k_y < 0$ (lower half, e.g., in figure 7(d-f)) propagate obliquely against the current. Thus, its wavelength will be compressed and correspondingly the wavenumber becomes larger. On the other hand, the wavelength of components of $k_y > 0$ will be stretched by the current, reducing their wavenumbers. At $\varphi = 180^o$, as shown in figure 7(p-r), the spectrum recovers to its symmetrical form, which however extends in k_x -direction compared with that without current, or in other words the major axis of the ellipse with the significant values of a spectrum is in k_x-direction. In addition, if one looks at the spectral peaks, their positions are almost unchanged for the cases with $\varphi = 90^o$ as they are for the cases without current. However, for the cases with $\varphi > 90^o$, the spectral peak shifts towards the higher wavenumber along the k_x-direction, e.g., in figure 7(g)(j)(m).

The nonlinear effects on the spectra with the presence of current need more discussions. Firstly, the nonlinearity itself does not visibly shift the position of the spectral peaks in the cases without current. With the presence of current, the nonlinearity tends to reduce the shift of the peak position, as clearly shown in figure 7(p-r), which will be discussed further in later section in a quantitative manner. Secondly, the nonlinearity tends to broaden the spectra near peaks when the current presents, as one can see from, e.g., figure 7(n) and (o), in particular with increase of incident angle. The broadening effect is consistent with what has been pointed out in many studies that when the wave steepness is large, the nonlinear interaction between wave modes generates a transfer of energy that modifies the wave spectrum and leads to the broadening of the directional spectrum towards high wavenumbers (Dysthe et al., 2003; Onorato et al., 2009).

The broadening effects can be quantified by the formula below (Hwang et al., 2000),

$$\sigma_2\left(k\right) = \sqrt{\frac{\int_{-\pi/2}^{\pi/2} \theta^2 \overline{D}\left(k,\theta\right) \mathrm{d}\theta}{\int_{-\pi/2}^{\pi/2} \overline{D}\left(k,\theta\right) \mathrm{d}\theta}} \tag{21}$$

where $\overline{D}\left(k,\theta\right)$ is the normalized distribution of the wavenumber spectrum and it can be evaluated by

$$\overline{D}\left(k,\theta\right) = \frac{S\left(k,\theta\right)}{\max\{S\left(k,\theta\right)\}} \tag{22}$$

Note that σ_2 is a function of k, therefore, to compare the spreading in terms of different current incident angles, the mean value of σ_2 around the peak wavenumber over the range $k/k_p = 0.8 \sim 1.2$ is employed (Hwang et al., 2000), which is denoted by σ_m and is estimated by using the formula

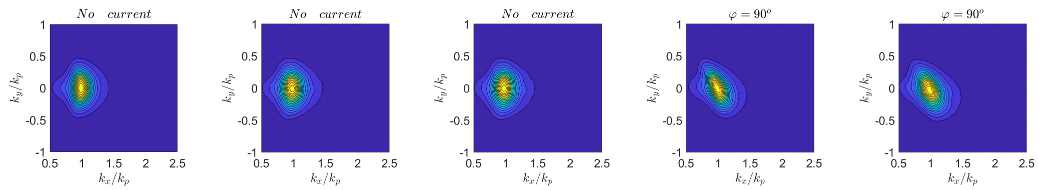

(a) (theo.) (b) ε_0=0.01(num.) (c) ε_0=0.15(num.) (d) (theo.) (e) ε_0=0.01(num.)

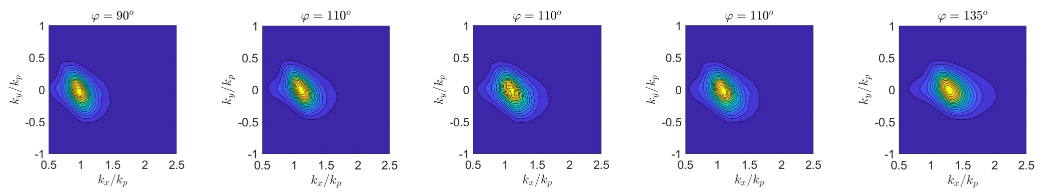

(f) ε_0=0.15(num.) (g) (theo.) (h) ε_0=0.01(num.) (i) ε_0=0.15(num.) (j) (theo.)

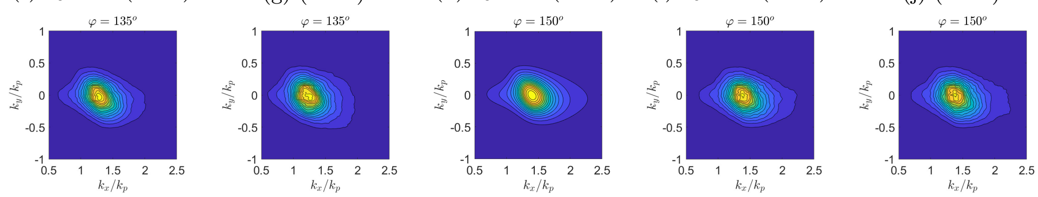

(k) ε_0=0.01(num.) (l) ε_0=0.15(num.) (m) (theo.) (n) ε_0=0.01(num.) (o) ε_0=0.05(num.)

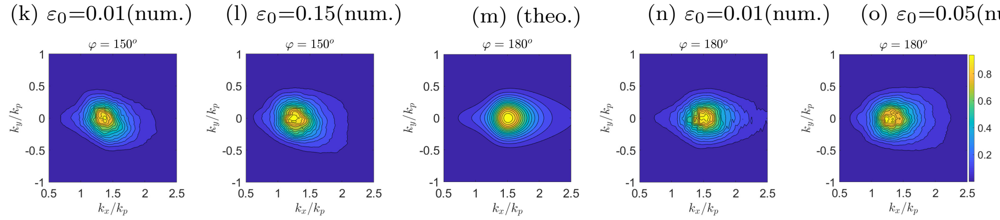

(p) ε_0=0.1(num.) (q) ε_0=0.15(num.) (r) (theo.) (s) ε_0=0.01(num.) (t) ε_0=0.15(num.)

Figure 7: Comparison of renormalized wavenumber spectra in terms of different current incident angles for $U_m/c_g \approx 0.3$. In the figure, (theo.) denotes the theoretical results and (num.) represents the numerical methods.(a-c): no current; (d-f): φ=90°; (g-i): φ=110°; (j-l): φ=135°; (m-q): φ=150°; (r-t): φ=180°

$$\sigma_m = \frac{1}{(1.2 - 0.8)\, k_p} \int_{0.8k_p}^{1.2k_p} \sigma_2\,(k)\, \mathrm{d}k. \tag{23}$$

As shown in figure 8, the mean value σ_m obtained by using the numerical results for the case $(k_p H_s)_0 = 0.01$ agrees very well with the theoretical predictions, where the maximum error is about 2.3% . It indicates that the numerical simulation of the small steepness waves successfully captured the variation of the spectral spreading due to the wave-current interactions when the nonlinearities are insignificant. The reduction of σ_m with increasing φ is also consistent with the observation in figure 7, where the presence of current stretches the spectra in the X-direction, thus reduces the directionality of the spectra when its incident angle increases. It is more interesting, however, to see that the spreading of the spectra becomes greater for the case $(k_p H_s)_0 = 0.15$ with the current incident angle being larger than 110°. The increment of the difference is more evident with the increase of φ . This also confirms the observation in figure 7, where the nonlinearities contribute to broadening the spectra, and the broadening effects are more significant for larger current incident angle. For example, the measurement of the spreading σ_m is enhanced by 15.6% for the case $\varphi = 180°$ due to the nonlinearities. Meanwhile, for fixed current incident angle $\varphi = 150°$, it is not surprising that the same trend of broadening is observed with increasing initial wave steepness. This confirms that the broadening effects are associated with the wave steepness, which will be further discussed in section 3.3.3.

3.3.2. Total spectral energy

When the waves propagate against an adverse or obliquely opposed current, the wave amplitudes will be enhanced. Since the spectral energy is associated with the square of the wave amplitude, the spectral energy will also grow as a result. Therefore, it is interesting to examine the effects of the current on the variation of the total spectral energy. To do so, we use the ratio of total spectral energy with presence of current over that without current, i.e., $E^{(c)}/E^{(0)}$, to represent the enhancement of the energy due to current. The total spectral energy $E^{(c)}$ with current and $E^{(0)}$ without current based on the numerical simulation results can be estimated by using the wavenumber spectra obtained in section 3.3.1. It can be found in figure 9 that the ratio $E^{(c)}/E^{(0)}$ for the case $(k_p H_s)_0 = 0.01$ are perfectly consistent with the theoretical predictions, and that the curve grows monotonically with the increase

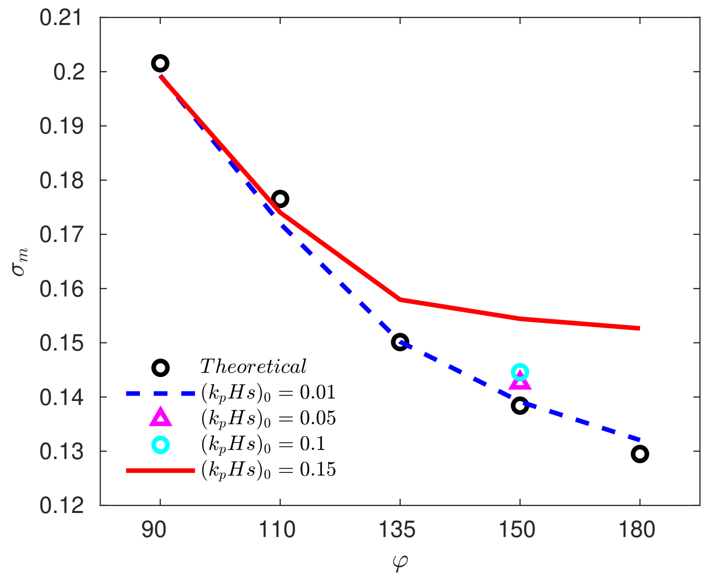

Figure 8: Magnitude of spreading versus current incident angle.

of the current incident angle. At the current of $\varphi = 180^{\circ}$, the total spectral energy can be 3 times larger than that with waves only.

For larger steepness waves, however, the curve representing the enhancement of the total spectral energy sits well below the theoretical predictions due to the nonlinear effects as shown in the figure. This finding is in fact consistent with the observations of unidirectional waves by Hjelmervik and Trulsen (2009), where it is reported that the nonlinearities can reduce the enhancement of the significant wave height, which approximately equals to four times the square root of the total spectral energy. Therefore, it is shown in figure 9 that $E^{(c)}/E^{(0)}$ for $(k_pH_s)_0 = 0.15$ exhibits a deceleration when φ increases, whereas it can only be enhanced by 2 times when the current incident angle reaches $\varphi = 180^{\circ}$. In addition, the reduction to the total spectral energy is found to be associated with initial wave steepness as indicated by the results for fixed current incident angle $\varphi = 150^{\circ}$. Larger steepness leads to reduced enhancement to the total spectral energy and such changes due to nonlinearities will be explained in section 3.3.3.

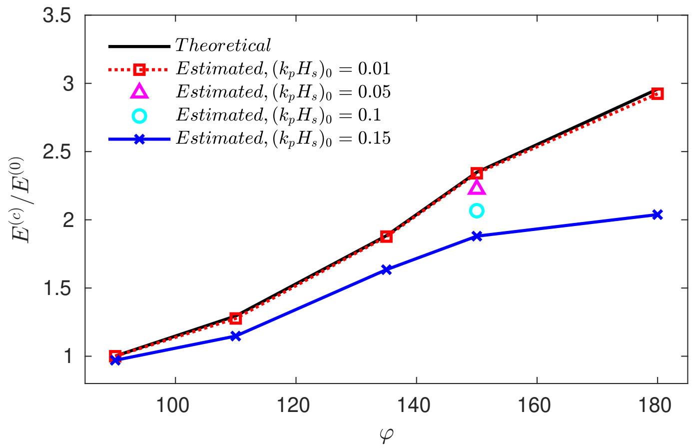

Figure 9: Spectral energy ratio with respect to the current incident angle.

3.3.3. Shift of the peak wavenumber

As indicated above during the discussion for figure 7, the peak wavenumber is shifted due to the wave-current interactions. The shift of the peak wave number for linear waves can be quantified by the following equation (Lavrenov, 2003)

$$\frac{k_p}{k_{p0}} = \frac{4}{\left[1 + \sqrt{1 + U' \cos\varphi}\right]^2} \tag{24}$$

where k_{p0} and k_p are peak wavenumbers before and after shift, respectively. It indicates that for a non-zero current speed, when the current incident angle φ increases, the peak wavenumber will shift to the higher end, which implies that the waves will become shorter. However, equation (24) only applies to small steepness waves as it is derived based on the linear theory. To examine the effects of nonlinearities on the shift of the peak wavenumber, one needs to look at the results obtained from the fully nonlinear simulations of larger steepness waves. These ratios of k_p/k_{p0} extracted from the wavenumber spectra of fully nonlinear simulations given in section 3.3.1 are shown in figure 10 together with the theoretical predictions of k_p/k_{p0} based on equation (24). It can be found in figure 10 that the results for small steepness waves based on the fully nonlinear simulations agree very well with the theoretical predictions based on equation (24). It is also found that with the increase of the current incident angle, the peak wavenumber becomes larger and can be amplified by a factor of 1.53 when φ =180°. For larger steepness waves, three points should be discussed. Firstly, the peak wavenumber is down shifted by about 3% without the presence of current compared with its linear counterpart. This is because the nonlinear interactions between the wave modes redistribute the spectral energy, which has been pointed out in many studies (Onorato et al., 2002; Dysthe et al., 2003; Toffoli et al., 2010). Secondly, with the increase of the current incident angle, the peak wavenumber is enhanced, but the enhancement is much below the linear predictions and seems to stabilize after φ exceeding 135°. For example, the amplification to the peak wavenumber reaches the maxima of $k_p/k_{p0} \approx 1.25$ when $\varphi = 135^{\circ}$ and 150°, while slightly reduces to $k_p/k_{p0} \approx 1.22$ when $\varphi = 180^{\circ}$. Lastly, it also implies that the reduction in the enhancement of the peak wavenumber due to nonlinearities becomes more evident when the current incident angle increases for large steepness waves. Meanwhile, this reduction of enhancement is also observed with increasing initial steepness for a fixed current incident angle $\varphi = 150^{\circ}$. Note that the reduction relative to the linear cases can reach 20.3% in presence of current with incident angle of $\varphi = 180^{\circ}$, which is significantly larger than 5% as reported in Toffoli et al. (2010) without considering the current.

Furthermore, the amplification of wave steepness, i.e., the ratio $k_pH_s/(k_pH_s)_0$, against the current incident angle is presented in figure 11, where the significant wave height is estimated by using $H_s = 4\sqrt{m_0}$ where m_0 equals to the total spectral energy obtained in section 3.3.2. It can be found that the ratio $k_pH_s/(k_pH_s)_0$ obtained by using the numerical results agree very well with the theoretical predictions, and can reach to 2.6 for $\varphi = 180^o$ for the cases with small wave steepness. For the cases with larger steepness, the enhancement of the ratio is less than the linear waves, with the maximum enhancement observed for $\varphi = 180^o$ being $k_pH_s/(k_pH_s)_0 \approx 1.8$. And this reduction of enhancement is more evident with increasing initial steepness for a fixed current incident angle. However, one may notice the ratio of the steepness of nonlinear waves to that of linear wave will be $(k_pH_s)_{\mathrm{nonlinear}}/(k_pH_s)_{\mathrm{linear}} = (0.15\times1.8)/(2.6\times0.01) \approx 10.4$, which indicate that the nonlinear waves are much steeper than the linear ones.

In general, the spreading of the spectra is reduced when current incident angle increases, and the reduction is less evident for larger steepness waves. The latter is due to the nonlinear energy transfer to higher wavenumber components(Dysthe et al., 2003; Onorato et al., 2009) and known as the weak wave turbulence (Fadaeiazar et al., 2018, 2020), which broadens the

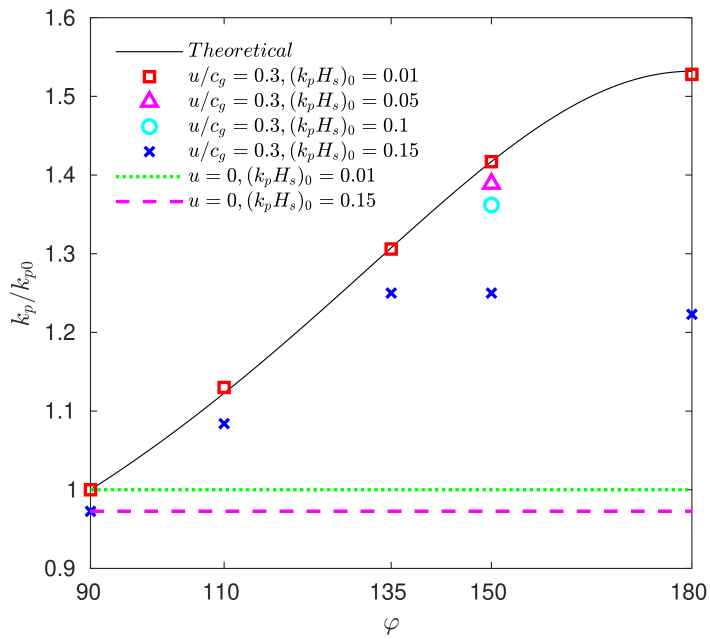

Figure 10: Shift of the peak wavenumber with respect to current incident angle (the dotted and dashed lines are for the cases without current.

spectra leading to mitigated reduction to the spreading. On the other hand, with increasing current incident angle, the total spectral energy (or significant wave height), peak wavenumber and wave steepness are enhanced, while the extent of the enhancement is suppressed for the larger steepness cases due to nonlinearities. The reasons can be summarized as follows. Firstly, it is understandable that the strength of the wave nonlinearities indicated by the BFI is associated with the wave steepness for a given bandwidth. It implies that the nonlinearities become stronger when initial steepness increases for a fixed current angle, or when incident angle increases for a given initial steepness. The latter is attributed to the current-induced compression to the incoming waves. Secondly, it is known that the nonlinearities play important role in downshifting the peak wavenumber in strong nonlinear cases causing the reduction of the enhancement to the peak wavenumber in presence of current. Consequently, the enhancement to the total spectral energy will also be reduced based on the conservation law of wave action. The changes to the peak wavenumber and total spectral energy(or significant wave height) lead to decelerated growth of wave steepness with increasing nonlinearities. In addition, the enhancement to the total spectral energy is also bounded by wave breaking for initially large steepness waves, thus the enhancement cannot be as arbitrarily large as predicted by linear theory.

3.4. Average shape of extreme waves with presence of current

In this subsection, the average shape of the extreme waves in directional seas subject to different current incident angles will be examined. To approximate the average shape of extreme waves, the criterion, i.e., $H/H_s > 2$ and $H_c/H_s > 1.2$, where H and H_c are the total (crest to trough) height and crest height (Kharif et al., 2009), is employed to detect a rogue wave. During the numerical simulation, we monitor the variation of the free surface in time within the whole computational domain for rogue wave occurrences. If an individual wave meets this criterion, its instant surface profile will be extracted and added to the database of samples, which are used for estimating the average shape after the sampling is completed and are denoted by $\eta_{NW}^{(ca)}$. Note that the average shape derived in such a way can contain the effects of fully nonlinear wave-wave and wave-current interactions.

3.4.1. Qualitative examination on the averaged extreme wave profiles

To demonstrate the effects of current incident angles on the average shape, results of $\eta_{NW}^{(c)}$ based on NewWave theory, i.e., given by equations (2)∼(6),

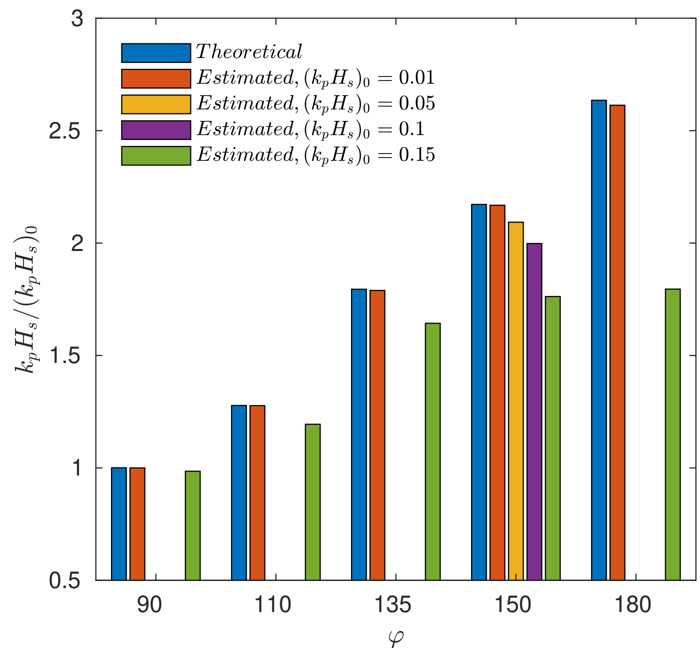

Figure 11: Amplification of the wave steepness.

and $\eta_{NW}^{(ca)}$ for both the cases $(k_pH_s)_0 = 0.01$ and 0.15 are presented in figure 12, where the origins of the horizontal axes are centered at the central crest peak. In general, it is observed that the contours of the average shape of numerical results for the cases of $(k_pH_s)_0 = 0.01$ are visually very similar to $\eta_{NW}^{(c)}$. It can also be found that when there is no current the three peaks of the preceding, central and following waves are on a straight line, which is largely aligned with the X-direction. When the waves are subject to current, the relative position of the three peaks depends on its incident angle and the steepness. For the waves of smaller steepness ($(k_pH_s)_0$ =0.01) on current, the three peaks are also on a line, though the relative direction of the line to X-direction are anti-clockwise rotated, depending on the current incident angle. When the waves are subject to the current with 90° incident angle, the three peaks are still on a line, which is rotated anti-clockwise. Such changes of the average shape can be attributed to the refraction as the current can refract the waves towards the current direction (Nwogu, 1993). For the waves of the larger steepness ($(k_pH_s)_0$ =0.15) on current with an angle of $\varphi = 110^{\circ}$, 135° or 150°, the relative positions of the three peaks are very different from other cases. They do not stay on a line but on a curve, whose curvature at the central peaks depends on the current incident angle, and the largest one occurs at $\varphi = 135^{\circ}$. For $\varphi = 180^{\circ}$ and $(k_pH_s)_0$ =0.15, the preceding peak is split into two small peaks, and thus one sees 4 peaks which appear as 'Y' shape, as shown in figure 12(r). This group asymmetry depicted by the disappearance of the preceding peak is due to nonlinear evolution of the prominent crest moving towards the front of the group at the focusing time (Gibbs and Taylor, 2005), which will be further discussed below.

On the other hand, by looking at the width of the contours near the central peak, one finds that with the increase of current incident angle, the width of the contours in X-direction becomes narrower. This is consistent with the discussions about the peak wavenumber in section 3.3.3, where the peak wavenumber is enhanced with larger current incident angle, thus the wave lengths are compressed consequently rendering a narrower crest. Furthermore, for the waves with larger steepness, the nonlinear effects of wave-wave and wave-current interactions yield a significant different average shape of extreme waves. Firstly, the width of the contours is much narrower than those for the smaller steepness. In addition, the preceding waves before the central crest for the larger steepness are significantly suppressed, compared with those for smaller steepness under the same current, as shown, e.g., in figure 12(n) and (o). This change in the average shape of extreme waves cannot be predicted by using the linear theory, therefore it is caused by the nonlinear wave-wave and wave-current interaction. This will be further discussed below.

To have a better visualization of the average shape of extreme waves, we examine the sectional wave profiles in X- and Y-direction, respectively. The wave profiles along $Y = 0$ and $X = 0$ are extracted from the results in figure 12, and they are plotted in figure 13. For the cases with smaller steepness, as can be seen from figure 13(a-d), numerical profiles are very similar to these predicted by the linear theory. Basically, they are symmetrical with respect to $X = 0$ and $Y = 0$, though the wavelength decreases with increase of current incident angle, being consistent with the observation by Gibbs and Taylor (2005) for simulating the directional focusing of a Gaussian shape wave group without current.

More interesting features can be observed in figure 13(e-f) for the cases with larger steepness. Firstly, the symmetry of the profiles for $\varphi > 90^o$ about Y=0 does not exist anymore. More specifically, the profile on X>0 (right) side is steeper than on the X<0 (left) side; the trough on the right is shallower than on the left in particular for $\varphi = 135^o \sim 180^o$; and the trough point on the right is closer to X=0 than that on the left. This asymmetry feature will be quantified and discussed in the next subsection. Secondly, the peaks on the right side, also for $\varphi > 90^o$, are much smaller, i.e., the waves being much flatter for the cases with the larger incident angle. Thirdly, the profiles in Y-direction (right column in figure 13) becomes significantly narrower for the cases with $\varphi > 90^o$. The above three phenomena can be caused by wave nonlinearity as indicated by Gibbs and Taylor (2005). However, the new finding here is that the nonlinear interaction between waves and current with incident angle $\varphi > 90^o$ can also cause the phenomena, even the wave nonlinearity is not strong. This is evidenced by what is shown in figure 13, in which one has found that the phenomena are not very visible for the cases with larger steepness but without current or current of $\varphi = 90^o$ neither for the cases with smaller steepness and with current, but only found in the cases with larger steepness and current of $\varphi > 90^o$. In addition, it is noted that more evident asymmetry of the wave profile is observed not only with increasing current incident angle, but also with the larger initial steepness, as illustrated in figure 13 (g) and (h). Such nonlinear changes of the average shape are the results of combined third-order near-resonant and resonant processes (Gibbs and Taylor, 2005). As the strength of these

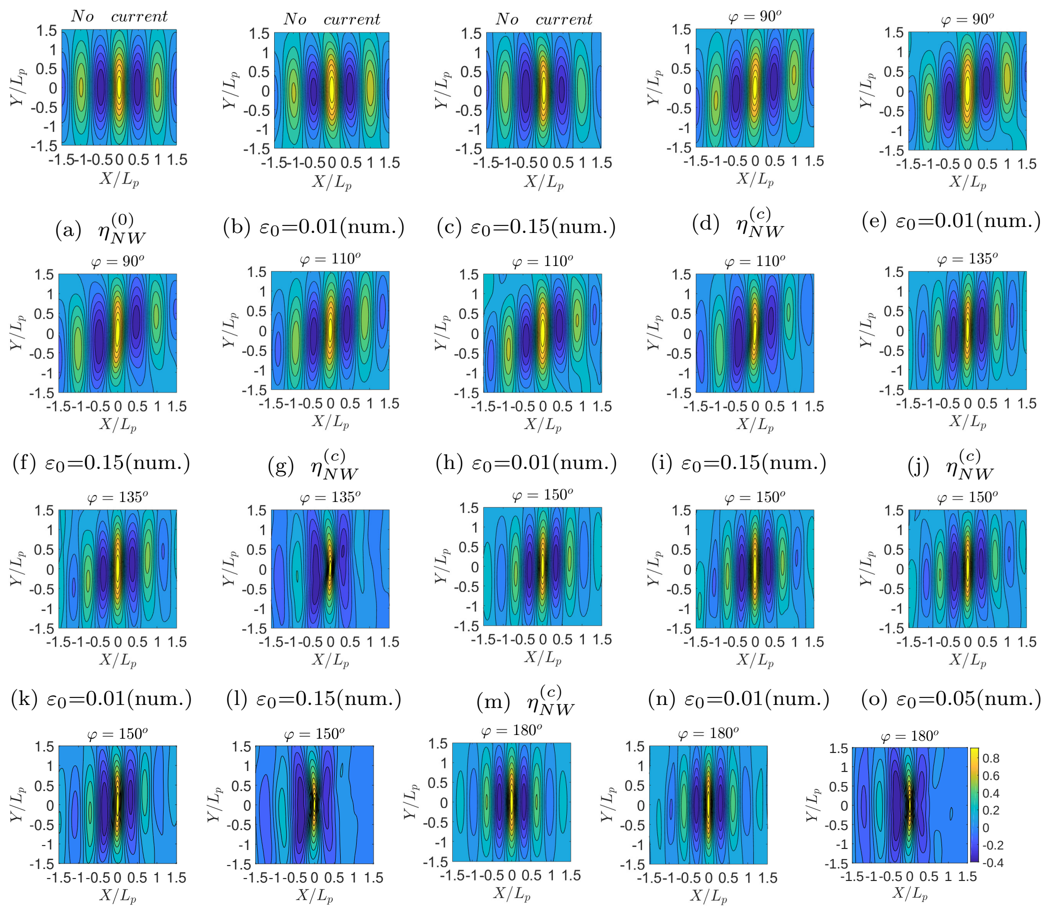

(a) $\eta_{NW}^{(0)}$ (b) ε_0=0.01(num.) (c) ε_0=0.15(num.) (d) $\eta_{NW}^{(c)}$ (e) ε_0=0.01(num.)

(f) ε_0=0.15(num.) (g) $\eta_{NW}^{(c)}$ (h) ε_0=0.01(num.) (i) ε_0=0.15(num.) (j) $\eta_{NW}^{(c)}$

(k) ε_0=0.01(num.) (l) ε_0=0.15(num.) (m) $\eta_{NW}^{(c)}$ (n) ε_0=0.01(num.) (o) ε_0=0.05(num.)

(p) ε_0=0.1(num.) (q) ε_0=0.15(num.) (r) $\eta_{NW}^{(c)}$ (s) ε_0=0.01(num.) (t) ε_0=0.15(num.)

Figure 12: Comparison between the averaged extreme wave contours. (a∼c) No current, (d∼f) φ =90$^{\rm o}$, (g∼i) φ =110$^{\rm o}$, (j∼l) φ =135$^{\rm o}$, (m∼q) φ =150$^{\rm o}$, (r∼t) φ =180$^{\rm o}$.

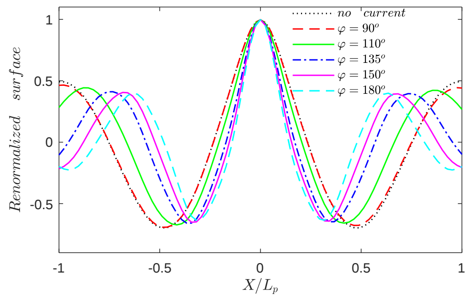

(a) $Y = 0$, theoretical $\eta_{NW}^{(c)}$

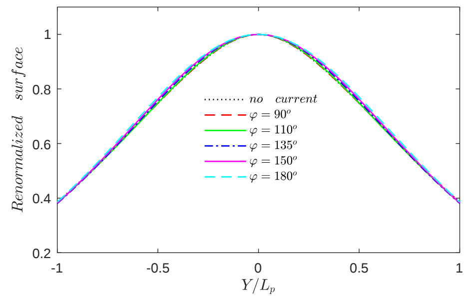

(b) $X = 0$, theoretical $\eta_{NW}^{(c)}$

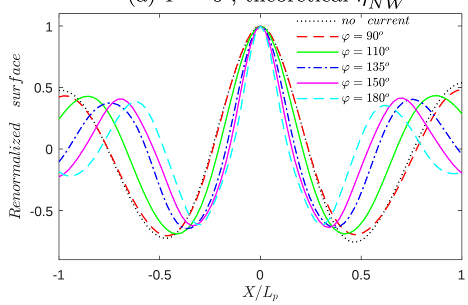

(c) $Y = 0$, $(k_p H_s)_0 = 0.01$

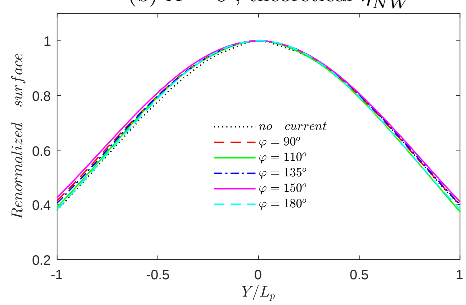

(d) $X = 0$, $(k_p H_s)_0 = 0.01$

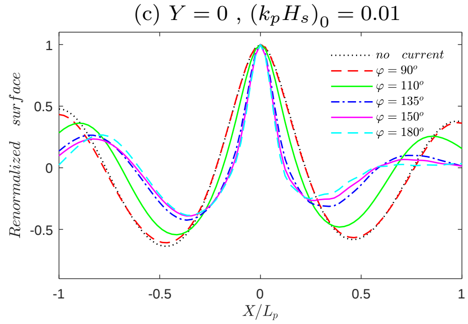

(e) $Y = 0$, $(k_p H_s)_0 = 0.15$

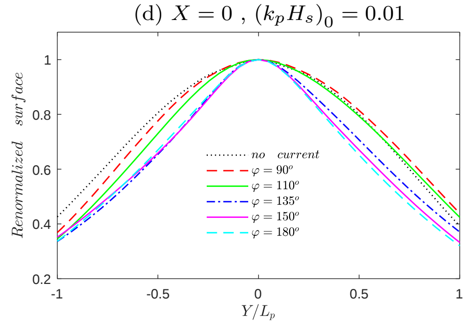

(f) $X = 0$, $(k_p H_s)_0 = 0.15$

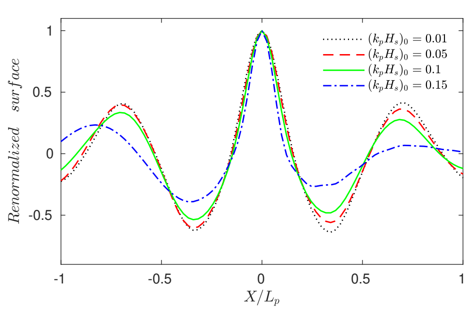

(g) $Y = 0$, $\varphi = 150^o$

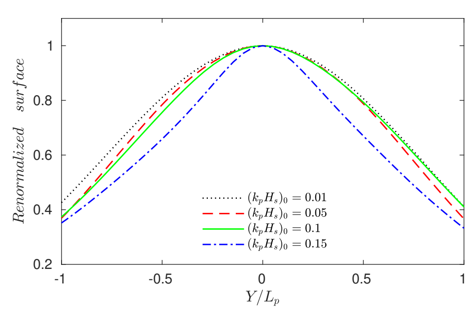

(h) $X = 0$, $\varphi = 150^o$

Figure 13: Average extreme wave profiles along X- and Y-direction.

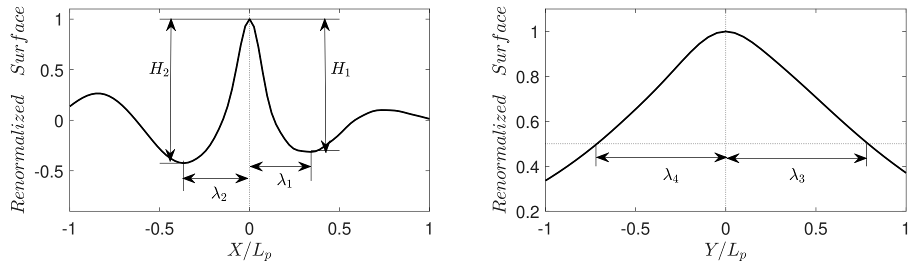

(a) $Y = 0$ (b) $X = 0$

Figure 14: Illustration of the horizontal asymmetry parameters.

processes are strongly associated with the BFI, it is understandable that the enhanced steepness and reduced spreading with increasing current incident angle or initial steepness will produce a larger BFI. Thus, it is prone to trigger these nonlinear processes leading to stronger nonlinear evolution of the wave groups and more apparent asymmetry of their average shapes.

3.4.2. Quantification of the asymmetrical wave profiles

To quantify the asymmetry of the average extreme wave profiles, we now introduce the following parameters

$$\xi_1 = \frac{H_1}{H_2},\ \xi_2 = \frac{\lambda_1}{\lambda_2} \text{ and } \xi_3 = \frac{\lambda_3}{\lambda_4}, \tag{25}$$

where the parameters H_1, H_2, λ_1, λ_2, λ_3 and λ_4 are defined in figure 14, in which λ_3 and λ_4 are the partial width of the wave crest in the Y-direction measured at the half crest height. From this figure, one can see that ξ_1 and ξ_2 denote the asymmetry of the wave profiles in X-direction (Y=0) while ξ_3 is the indicator of the asymmetry of the wave profiles in Y-direction (X=0).

The values of ξ_1 , ξ_2 and ξ_3 are estimated based on the wave profiles in figure 13. They are summarized in table 1 and plotted in figure 15. It can be found in figure 15 that for all the cases with smaller steepness waves, $\xi_1 \approx 1$, $\xi_2 \approx 1$ and $\xi_3 \approx 1$, no matter the current is in presence or not. However, for the cases with larger steepness waves, the different parameters have different behaviors depending on the current direction. Without current or with current at an incident angle of 90$^\text{o}$, the value $\xi_1 \approx 0.97$ as seen in figure 15(a). When the angle increases, in particular $\varphi > 110^\text{o}$, the value of ξ_1 becomes much smaller, as low as 0.90 at $\varphi > 180^\text{o}$. As for ξ_2 shown in figure 15(b), it equals to about 1 for all the cases of smaller wave steepness

Initial steepness	$(k_pH_s)_0 = 0.01$			$(k_pH_s)_0 = 0.15$		
	ξ_1	ξ_2	ξ_3	ξ_1	ξ_2	ξ_3
No current	1.0000	1.0000	1.0000	0.9664	1.0000	0.9934
$\phi = 90^o$	0.9917	0.9908	1.0000	0.9739	1.0000	1.1181
$\phi = 110^o$	0.9916	1.0000	1.0000	0.9598	0.9422	1.1498
$\phi = 135^o$	0.9934	0.9944	1.0000	0.9214	0.9344	1.1031
$\phi = 150^o$	0.9946	1.0000	1.0000	0.9101	0.7350	1.0500
$\phi = 180^o$	0.9988	0.9943	1.0000	0.9033	0.7135	0.9972

Table 1: Summary of the horizontal asymmetry parameters for $\eta_{NW}^{(ca)}$.

or for the cases with current at the incident angle of 90^o. However, its value can be reduced to 0.7 for the cases with the larger wave steepness and with current at an incident angle of 150^o or 180^o. One more interesting point is that the ratio of the local steepness of the profile on $X > 0$ part to that of $X < 0$ part, $(H_1/\lambda_1)/(H_2/\lambda_2) = \xi_1/\xi_2$ is about 1.24 and 1.27 corresponding to φ=150^o and φ =180^o, respectively, for the cases of $(k_pH_s)_0$=0.15, indicating that the right profile is much steeper than the left one. The reduced ξ_1 and ξ_2 with increasing incident angle render a steeper right-half profile in mean wave direction for large steepness cases, which indicates the formation of "wall of water" due to the nonlinear evolution as explained earlier. As for ξ_3 shown in figure 15(c), its largest value, 1.15, occurs at φ =110^o of current for $(k_pH_s)_0$=0.15, among the cases studied, and it is equal about 1 for all the cases with smaller steepness and with φ =180^o. On the other hand, as shown in figure 15(d), these asymmetry factors deviate from 1 more apparently with increasing initial steepness when the current incident angle is fixed. The asymmetry becomes noticeable for the case $(k_pH_s)_0$=0.05 with ξ_1 less than 1, which depicts a shallower preceding trough ($H_1 < H_2$).

4. Discussions on suitability of NewWave theory

As demonstrated in section 3.4, the average profile $\eta_{NW}^{(c)}$ based on NewWave theory cannot well reflect the changes in the shape of extreme waves when wave steepness is large, in particular when incident angle of current is larger than 135^o. To further investigate this issue, another two methods for approximating the average shape of extreme waves based on NewWave theory

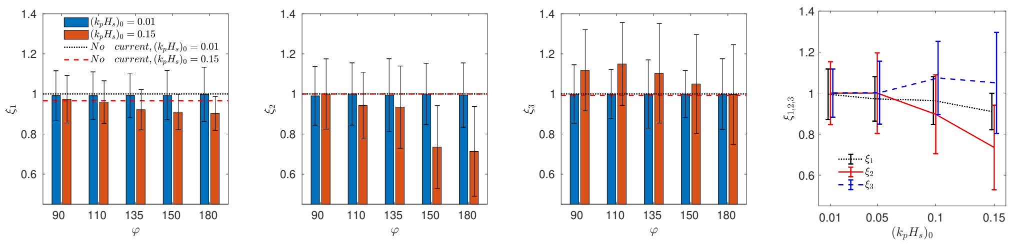

(a) ξ_1 against φ (b) ξ_2 against φ (c) ξ_3 against φ (d) ξ_i against $(k_pH_s)_0$

Figure 15: Comparison of the asymmetry parameters against current incident angle.

considering a certain degree of nonlinearity will be employed. These models have been introduced in section 2 and now are summarized again as below:

1. $\eta_{NW}^{(c)}$: the average shape of the extreme waves in space obtained directly by applying equation (2) to the spectrum based on equations (3)∼(6), which is based purely on the linear theory and neglects any nonlinearities.
2. $\eta_{NW}^{(c1)}$: the average shape obtained by applying equation (2) to the spectrum from the fully nonlinear simulations, in which the spectrum is a more accurate representation of the fully nonlinear wave-wave and wave-current interactions in comparison with method (i) but the conversion from spectrum to average shape is based on the linear theory.
3. $\eta_{NW}^{(c2)}$: obtained by equations (8) and (9) that consider second-order Stokes-type corrections to $\eta_{NW}^{(c)}$ and thus includes nonlinear bound wave effects up to the second-order.

The models (i) ∼ (iii) of approximating the average shape of extreme waves are known as the NewWave theory. They will be compared with $\eta_{NW}^{(ca)}$, which is the average shape of extreme waves estimated by using the results of fully nonlinear simulations as explained in the beginning of section 3.4.

4.1. On predicting the average extreme wave profiles

The sectional profiles of the average shape of extreme waves obtained by using methods (i)∼ (iii) with $\eta_{NW}^{(ca)}$ are depicted in figure 16. One may find that for small steepness waves, the profiles of $\eta_{NW}^{(c)}$ (very close to $\eta_{NW}^{(c2)}$ which is not presented) and $\eta_{NW}^{(ca)}$ agree very well in both X- and Y-direction, which indicates that the models (i)∼ (iii) based on NewWave theory can be successfully employed to predict the average shape of extreme waves when the wave steepness is small with or without current. However, for the waves with larger steepness, the profiles of model (i)$\sim$ (iii) based on the NewWave theory start to exhibit their inefficacy. To be more specific, their limitations are summarized below:

1. Model (i), i.e., $\eta_{NW}^{(c)}$ does not well predict the features of the average shape induced by nonlinear interaction, such as the wavelength contraction (or peak wavenumber enhancement), asymmetry, the reduction of the crest width in both X- and Y-direction, the elevation of the wave trough and the suppression of the preceding wave with increasing current incident angle.
2. Model (ii), i.e., $\eta_{NW}^{(c1)}$, does not greatly improve the results of $\eta_{NW}^{(c)}$, which means that the major cause of difference in the average shape of extreme waves is the relation between the spectrum and wave shapes, i.e. equation (2), but not the spectrum used in that equation.
3. Method (iii), i.e., $\eta_{NW}^{(c2)}$, gives the average shapes which are closer to $\eta_{NW}^{(ca)}$ than the other two models, in particular in Y-direction, though significant difference between $\eta_{NW}^{(c2)}$ and $\eta_{NW}^{(ca)}$ for large steepness waves can still be observed. Again, this method cannot sufficiently reveal the asymmetrical profile in X-direction or the suppression of the preceding wave, as well as other features caused by nonlinear interaction between waves and current.

To show the sensitivity of the accuracy of the NewWave models on wave steepness, the sectional profile in X-direction of $(k_pH_s)_0$ =0.05 and 0.1 for φ =150° are presented in figure 17. It shows that the deviation between the theoretical predictions and numerical results becomes more significant with increasing wave steepness, which is understandable as the NewWave models become less accurate for stronger nonlinear cases. Nevertheless, it is noted that though $\eta_{NW}^{(c2)}$ leads to better approximation of the average profile, it still cannot describe the asymmetry feature which is already noticeable from the simulated profile regarding the case $(k_pH_s)_0$ =0.05.

4.2. On predicting the vertical asymmetry factor

To quantify the asymmetry features of wave profiles, Soares et al. (2003) had introduced a parameter that calculates the ratio between the extreme crest height and the nearest trough depth. They pointed out that observations during storm sea state in the North Sea indicates that this ratio is scattered

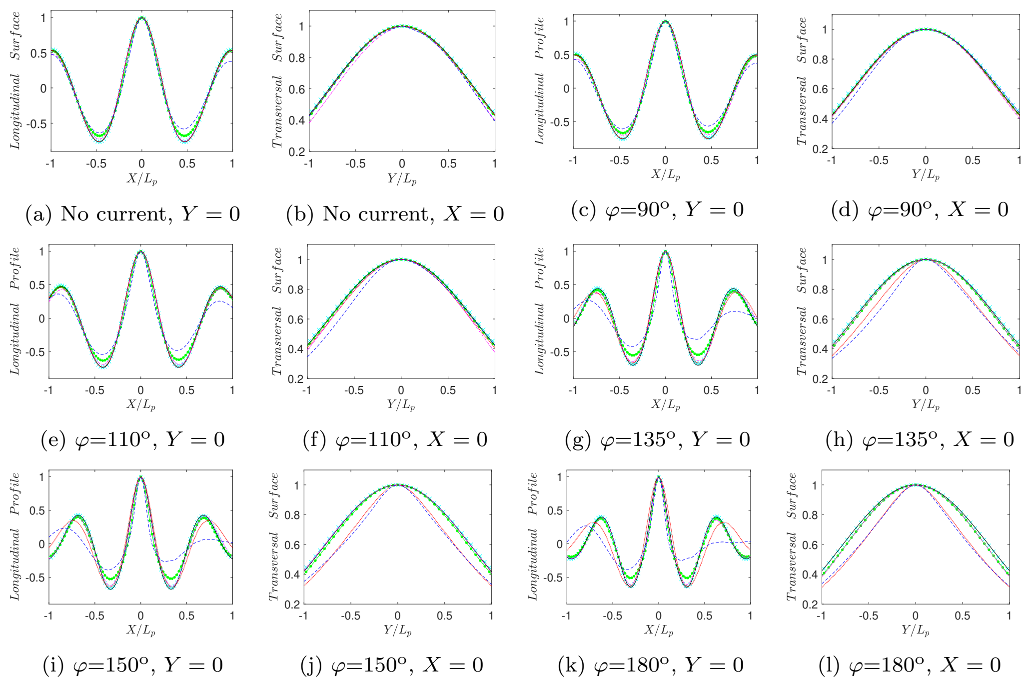

(a) No current, $Y = 0$ (b) No current, $X = 0$ (c) φ=90°, $Y = 0$ (d) φ=90°, $X = 0$

(e) φ=110°, $Y = 0$ (f) φ=110°, $X = 0$ (g) φ=135°, $Y = 0$ (h) φ=135°, $X = 0$

(i) φ=150°, $Y = 0$ (j) φ=150°, $X = 0$ (k) φ=180°, $Y = 0$ (l) φ=180°, $X = 0$

Figure 16: Comparisons of the average extreme wave profiles. "x": $\eta^{(c)}_{NW}$, "——": $\eta^{(c1)}_{NW}$ for $(k_pH_s)_0$= 0.01; "- · - · -": $\eta^{(ca)}_{NW}$ for $(k_pH_s)_0$=0.01; " . . . . . . ": $\eta^{(c1)}_{NW}$ for $(k_pH_s)_0 = 0.15$; "– ● –" : $\eta^{(c2)}_{NW}$ for $(k_pH_s)_0 = 0.15$, "- - - -" : $\eta^{(ca)}_{NW}$ for $(k_pH_s)_0$= 0.15.

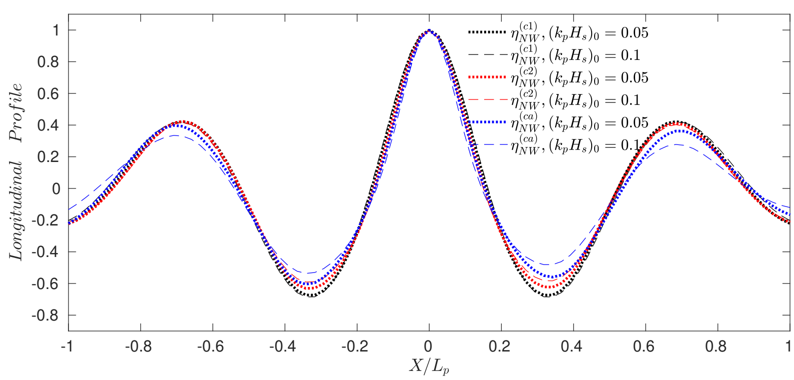

Figure 17: Average extreme wave profiles of various steepness for φ=150°.

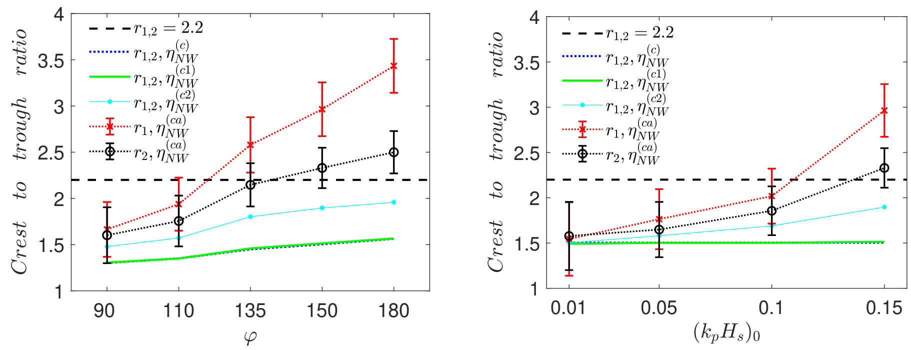

(a) Fixed $(k_pH_s)_0 = 0.15$

(b) Fixed φ= 150^{o}

Figure 18: Vertical asymmetry indicator versus (a) current incident angle and (b) initial wave steepness.

around 2.2 regardless whether current is in presence. Inspired by that, we introduce two parameters to represent the asymmetry features of average shapes of the extreme waves given by different models, i.e.,

$$r_1 = \frac{H_c}{H_{tf}} \text{ and } r_2 = \frac{H_c}{H_{tb}} \tag{26}$$

where H_{tf} and H_{tb} denote the trough height (vertical distance from the lowest point to mean level) in the preceding and following sides of the central crest, respectively, which are extracted from figure 12. The values of r_1 and r_2 are calculated by using the averaged shape of the extreme waves for the case $(k_pH_s)_0$=0.15 and the results are presented in figure 18(a), also with the observation by Soares et al. (2003), i.e., $r_{1,2} = 2.2$. Since it has been observed in figure 16 that for small steepness waves, the values of r_1 and r_2 by using models (i)$\sim$ (iii) are expected to be very similar to that obtained by fully nonlinear simulations, only the cases for larger initial steepness are presented in the figure. While the results for fixed current incident angle considering varying initial steepness are displayed in figure 18(b).

In general, for fixed initial steepness, the values of r_1 and r_2 indicated by the lines denoting $\eta_{NW}^{(ca)}$ grow rapidly as current incident angle increases, with a minimum of $r_1 = 1.67$ and $r_2 = 1.60$ for $\varphi = 90^{o}$, while they can reach the maxima of $r_1 = 3.43$ and $r_2 = 2.50$ for $\varphi = 180^{o}$. The vertical asymmetry factors scattering around 2.2 agrees reasonably well with the in-situ observation, indicating that the nonlinear numerical simulations successfully captured the vertical asymmetry features of the extreme waves. It should be noticed that in the cases, the curve of r_1 is higher than r_2, which is because the preceding trough is relatively shallower than the following one, as shown in figure 13(e). It is also noted that the big value of r_1 indicates that the wave is more like a wall of water for a viewer in front of it as observed in reality (Gibbs and Taylor, 2005; Lindgren, 2006). On the other hand, for fixed current incident angle, the values of r_1 and r_2 grow as the initial steepness increases with the minimum of $r_1 = r_2 = 1.5$ appearing at $(k_pH_s)_0$=0.01. The two curves deviate from each other with r_1 being slightly larger as the initial steepness increases.

Though models (i)∼ (iii) based on the NewWave theory predict the growing trend of r_1 and r_2 with increasing φ , but they do not reflect the fact of $r_1 \neq r_2$. This limitation of the NewWave models has been reported by Walker et al. (2004) that even included nonlinear Stokes-type corrections to the fifth order. Moreover, the models (i) and (ii) significantly underestimate the values for r_1 and r_2 . For the current in adverse direction, i.e., $\varphi = 180^o$, they underpredict r_1 and r_2 by 55% and 38% , respectively, in comparison with those for $\eta_{NW}^{(ca)}$, despite that they only provide accurate approximation for the cases of small steepness $(k_pH_s)_0$=0.01. The model (iii) is slightly better. For instance, the difference in the values of r_1 and r_2 predicted by using the model (iii) and those for $\eta_{NW}^{(ca)}$ becomes 43% and 22% , respectively for the case $\varphi = 180^o$. In addition, the values of the asymmetrical factors given by all the three models are lower than 2.2 in all the cases, inconsistent with the observation in reality; thus, they should not be used to predict the vertical asymmetry parameters when the nonlinearity in the wave-current interaction is strong.

5. Conclusion

This paper presents a study on the properties of extreme waves in directional seas subjected to current in different directions using fully nonlinear numerical simulations. The spatiotemporal scale is quite large to allow the nonlinear interaction between waves and current to well develop. For each case with a given initial wave steepness and current incident angle, four realizations are performed with different sequences of random numbers in computing the phases of wave components. Each simulation lasts for 500 peak periods, and about 5×10^4 waves are collected from the probes in each simulation for achieving reliable statistical analysis. A broad range of extreme wave properties are analyzed and investigated, including how the current affects the kurtosis, crest exceedance probability, spectral properties and average shapes of extreme waves. The study is also extended on the suitability of three models established by using the NewWave theory which is widely employed to describe the average shape of extreme waves. Some interesting findings are summarized as below.

For the waves with strong nonlinearity, the nonlinear wave-current interactions have significant impacts on the wave statistics and spectral properties. These include that 1) current significantly enhances the wave crest exceedance probability at distribution tail, which is much larger than the prediction of the existing second-order models and that the extent of enhancement depends on the incident angle of current. The maximum enhancement occurs at the incident angle of 135^{o} but not at 180^{o}, in the cases studied; 2) the maxima of the kurtosis occurs perhaps at a current incident angle less than 180^{o}, being 135^{o} in the cases studied in this paper, implying that the probability of rogue waves occurrence may be high under the condition; 3) current with its incident angle being larger than 110^{o} broadens the spectra; 4) current causes the severe vertical and horizontal asymmetry of extreme wave profiles, such as different steepness on two sides of an extreme wave peak, and different wave crests and different troughs before and after the extreme wave; 5) these non-Gaussian behaviours in wave statistics and spectral properties are more evident with increasing initial wave steepness when current incident angle is fixed. It is interesting to notice that the nonlinear wave-current interaction can make the crest much higher than surrounding surface, which becomes more evident for larger current incident angle, showing the possibility of the 'wall of water' nature of rogue waves in reality (Gibbs and Taylor, 2005).

To study the suitability of the NewWave theory for describing the average shape of extreme waves in directional seas with current, three methods based on the theory are established and investigated. Method (i) employs the linearly predicted spectra and a linear spectrum-to-wave profile conversion theory (i.e., equation (2)); Method (ii) uses the spectra obtained from the fully nonlinear numerical simulations and equation (2); Method (iii) adopts the linearly predicted spectra but a nonlinear spectrum-to-wave profile conversion theory considering the Stokes-type corrections (i.e. equation (8)). It is found that all three methods can successfully predict the average extreme wave profiles no matter if the current presents or not when the initial wave steepness is small (i.e., initial wave steepness $(k_pH_s)_0 = 0.01$ in this paper). This confirm that these methods are robust under weak or moderate wave-current interaction. However, they become incapable to give acceptable results for the cases of large steepness waves with presence of current, though the Method (iii) gives the results closer to the full nonlinear results than Method (i) and (ii). More specifically, Method (i) fails to predict the wavelength contraction, the reduction of the crest width in both X- and Y-direction, the elevation of the wave trough and the disappearance of the preceding wave with the increasing current incident angle. Method (ii) fails to describe the reduction of crest width, elevation of the trough in X-direction, and the disappearance of the preceding wave. Method (iii) cannot reveal the asymmetrical profile in X-direction or the suppression of the proceeding wave. All the methods significantly underestimate the vertical asymmetry parameter represented by equation (26), e.g., by $43\% \sim 55\%$ in the adverse current case.

It is expected that the above new findings enrich our understanding on the properties of extreme waves and also on the occurring mechanism of rogue waves when current presents. Nevertheless, the above conclusions are derived for a given spreading angle of directional waves and current speed, i.e., $N = 24$ and $U_m/c_g \approx 0.3$, though the cases are quite typical in reality. Further investigations on current with different speeds in oblique directions will be carried out in the future to shed more light on the properties of extreme waves encountering current. In addition, broader spectral bandwidth for the initial spectrum will be taken into consideration in the future study to investigate the effects of oblique current on initially broadband seas. Moreover, there has been growing interest recently in the waves interacting with current jet (Hjelmervik and Trulsen, 2009) or vertically sheared current of arbitrary vorticity (Nwogu, 2009; Ellingsen and Li, 2017; Yang and Liu, 2020). This could have significant implications in developing a better understanding of the dynamics of extreme waves in the region subject to strong wind driven surface current, which will be studied in the future.

Acknowledgements. The authors gratefully acknowledge the financial support of EPSRC, UK (EP/L01467X/1, EP/N006569/1, EP/N008863/1 and EP/M022382/1) and DST-UKIERI project (DST-UKIERI-2016-17-0029). Most of research involved in this paper was completed when the first author worked in City, University of London, under support of EP/L01467X/1.

Appendix A. Spectrum of directional waves with presence of current

Lavrenov (1998, 2003) pointed out that the spectral density of the energy wave action is preserved along the ray, i.e.,

$$N(\boldsymbol{k}) = N_0(\boldsymbol{k}_0) \tag{A.1}$$

where

$$\frac{S(\omega,\theta)}{\sigma} = N(\boldsymbol{k})\frac{\partial(k_x,k_y)}{\partial(\omega,\theta)} \tag{A.2}$$

Therefore, the following equation can be derived

$$S(\omega,\theta) = \frac{\partial k^2}{\partial\omega}\sigma\left(\frac{\partial k_0^2}{\partial\omega_0}\sigma_0\right)^{-1} S_0(\omega_0,\theta_0) = \frac{k\sigma}{k_0\sigma_0}\frac{\partial k/\partial\omega}{\partial k_0/\partial\omega_0}S_0(\omega_0,\theta_0) \tag{A.3}$$

It should be noted that in the case of non-uniform stationary current, the frequency remains constant along the wave propagation rays, i.e., $\omega = \omega_0$. While to determine the wavenumber in terms of the current speed, the solution to the equation (3) and (4) can be given by

$$k = \frac{4\omega^2}{g\left[1+\sqrt{1+U'\cos(\varphi-\theta)}\right]^2} \tag{A.4}$$

Differentiating equation (3) and (4) with respect to ω and incorporating equation (A.4) yields

$$\frac{\partial k}{\partial\omega} = \frac{4\omega}{g\sqrt{1+U'\cos(\varphi-\theta)}\left[1+\sqrt{1+U'\cos(\varphi-\theta)}\right]} \tag{A.5}$$

Substitute equations (A.4) and (A.5) into equation (A.3) leads to equation (3).

Appendix B. Formulations of the ESBI

The formulations of G_1 and G_2 are given as

$$F\{G_1\} = F\{V\} - KF\left\{\widetilde{\phi}\right\} - F\{\mu\} \tag{B.1}$$

$$F\{G_2\} = \frac{1}{2}F\left\{\frac{\left(V + \nabla\zeta\cdot\nabla\widetilde{\phi}\right)^2}{1+|\nabla\zeta|^2} - |\nabla\widetilde{\phi}|^2\right\} - F\{\psi\} \tag{B.2}$$

where

$$\begin{pmatrix} \mu \\ \psi \end{pmatrix} = \begin{pmatrix} \nabla\eta\cdot U + \eta\left(\nabla\cdot\boldsymbol{U}\right) \\ \nabla\widetilde{\phi}\cdot\boldsymbol{U} - \eta\left(\nabla\overline{\eta}\cdot\boldsymbol{U}\right)\nabla\cdot\boldsymbol{U} + \frac{1}{2}\left(\eta\nabla\cdot\boldsymbol{U}\right)^2 \end{pmatrix} \tag{B.3}$$

In addition, each part of the vertical velocity can be calculated by using

$$V_1 = F^{-1}\left\{KF\left\{\widetilde{\phi}\right\}\right\} \tag{B.4}$$

$$V_2 = -F^{-1}\left\{KF\left\{\zeta V_1\right\}\right\} - \nabla\cdot\left(\zeta\nabla\widetilde{\phi}\right) \tag{B.5}$$

$$V_3 = F^{-1}\left\{\frac{K}{2\pi}F\left\{\int\widetilde{\phi}'\left[1-\frac{1}{\left(1+D^2\right)^{3/2}}\right]\nabla'\cdot\left[\left(\zeta'-\zeta\right)\nabla'\frac{1}{R}\right]\mathrm{d}\boldsymbol{X}'\right\}\right\} \tag{B.6}$$

$$V_4 = F^{-1}\left\{\frac{K}{2\pi}F\left\{\int\frac{V'}{R}\left(1-\frac{1}{\sqrt{1+D^2}}\right)\mathrm{d}\boldsymbol{X}'\right\}\right\} \tag{B.7}$$

where $D = \left(\zeta'-\zeta\right)/R$, $R = |\boldsymbol{R}| = |\boldsymbol{X}'-\boldsymbol{X}|$, the variables with the prime indicate those at source point $(\boldsymbol{X}', Z')$, the variables without the prime are those at field point $(\boldsymbol{X}, Z)$. Note that V_3 and V_4 can be further written into convolutions up to seventh order, i.e.,

$$V_3 = \underbrace{V_3^{(1)}}_{\text{4th convolution}} + \underbrace{V_3^{(2)}}_{\text{6th convolution}} + \underbrace{V_{3,I}}_{\text{integration}} \tag{B.8}$$

$$V_4 = \underbrace{V_4^{(1)}}_{\text{3rd convolution}} + \underbrace{V_4^{(2)}}_{\text{5th convolution}} + \underbrace{V_4^{(3)}}_{\text{7th convolution}} + \underbrace{V_{4,I}}_{\text{integration}} \tag{B.9}$$

where the convolution parts of V_3 are given by

$$
\begin{aligned}
F\left\{V_3^{(1)}\right\} = & - \frac{K}{6}\Big[K\mathrm{i}\boldsymbol{K}\cdot F\left\{\zeta^3\nabla\widetilde{\phi}\right\} - 3F\left\{\zeta F^{-1}\left\{K\mathrm{i}\boldsymbol{K}\cdot F\left\{\zeta^2\nabla\widetilde{\phi}\right\}\right\}\right\} \\
& + 3F\left\{\zeta^2 F^{-1}\left\{K\mathrm{i}\boldsymbol{K}\cdot F\left\{\zeta\nabla\widetilde{\phi}\right\}\right\}\right\} \\
& + F\left\{\zeta^3 F^{-1}\left\{K^3 F\left\{\widetilde{\phi}\right\}\right\}\right\}\Big]
\end{aligned} \tag{B.10}
$$

$$
\begin{aligned}
F\left\{V_3^{(2)}\right\} = & - \frac{K}{120}\Big[\mathrm{i}\boldsymbol{K}K^3\cdot F\left\{\zeta^5\nabla\widetilde{\phi}\right\} - 5F\left\{\zeta F^{-1}\left\{\mathrm{i}\boldsymbol{K}K^3\cdot F\left\{\zeta^4\nabla\widetilde{\phi}\right\}\right\}\right\} \\
& + 10F\left\{\zeta^2 F^{-1}\left\{\mathrm{i}\boldsymbol{K}K^3\cdot F\left\{\zeta^3\nabla\widetilde{\phi}\right\}\right\}\right\} \\
& - 10F\left\{\zeta^3 F^{-1}\left\{\mathrm{i}\boldsymbol{K}K^3\cdot F\left\{\zeta^2\nabla\widetilde{\phi}\right\}\right\}\right\} \\
& + 5F\left\{\zeta^4 F^{-1}\left\{\mathrm{i}\boldsymbol{K}K^3\cdot F\left\{\zeta\nabla\widetilde{\phi}\right\}\right\}\right\} \\
& + F\left\{\zeta^5 F^{-1}\left\{K^5 F\left\{\widetilde{\phi}\right\}\right\}\right\}\Big]
\end{aligned} \tag{B.11}
$$

and the integration part

$$
\begin{aligned}
F\left\{V_{3,I}\right\} = & \quad \frac{K}{2\pi}F\Bigg\{\frac{35}{16}\int \widetilde{\phi}'\nabla'\cdot\left[\left(\zeta'-\zeta\right)\nabla'\frac{1}{R}\right]D^6\mathrm{d}\boldsymbol{X}' \\
& + \int \widetilde{\phi}'\big[1-\left(1+D^2\right)^{-3/2}-\frac{3}{2}D^2 \\
& + \frac{15}{8}D^4-\frac{35}{16}D^6\big]\nabla'\cdot\left[\left(\zeta'-\zeta\right)\nabla'\frac{1}{R}\right]\mathrm{d}\boldsymbol{X}'\Bigg\}
\end{aligned} \tag{B.12}
$$

Meanwhile, the convolution parts of V_4 are given by

$$
\begin{aligned}
F\left\{V_4^{(1)}\right\} = & - \frac{K}{2}\Big[KF\left\{\zeta^2 V\right\} - 2F\left\{\zeta F^{-1}\left\{KF\left\{\zeta V\right\}\right\}\right\} \\
& + F\left\{\zeta^2 F^{-1}\left\{KF\left\{V\right\}\right\}\right\}\Big]
\end{aligned} \tag{B.13}
$$

$$
\begin{aligned}
F\left\{V_4^{(2)}\right\} = & - \frac{K}{24}\big[K^3 F\left\{V\zeta^4\right\} - 4F\left\{\zeta F^{-1}\left\{K^3 F\left\{V\zeta^3\right\}\right\}\right\} \\
& + 6F\left\{\zeta^2 F^{-1}\left\{K^3 F\left\{V\zeta^2\right\}\right\}\right\} \\
& - 4F\left\{\zeta^3 F^{-1}\left\{K^3 F\left\{V\zeta\right\}\right\}\right\} \\
& + F\left\{\zeta^4 F^{-1}\left\{K^3 F\left\{V\right\}\right\}\right\}\big]
\end{aligned} \tag{B.14}
$$

$$
\begin{aligned}
F\left\{V_4^{(3)}\right\} = \quad & \frac{-K}{720}\left[K^5 F\left\{V\zeta^6\right\} - 6F\left\{\zeta F^{-1}\left\{K^5 F\left\{V\zeta^5\right\}\right\}\right\}\right. \\
+ \quad & 15F\left\{\zeta^2 F^{-1}\left\{K^5 F\left\{V\zeta^4\right\}\right\}\right\} \\
- \quad & 20F\left\{\zeta^3 F^{-1}\left\{K^5 F\left\{V\zeta^3\right\}\right\}\right\} \\
+ \quad & 15F\left\{\zeta^4 F^{-1}\left\{K^5 F\left\{V\zeta^2\right\}\right\}\right\} \\
- \quad & 6F\left\{\zeta^5 F^{-1}\left\{K^5 F\left\{V\zeta\right\}\right\}\right\} \\
+ \quad & \left. F\left\{\zeta^6 F^{-1}\left\{K^5 F\left\{V\right\}\right\}\right\}\right]
\end{aligned} \tag{B.15}
$$

and the integration part

$$
F\left\{V_{4,I}\right\} = \frac{K}{2\pi}F\left\{\int \frac{V'}{R}\left(1 - \frac{1}{\sqrt{1+D^2}} - \frac{1}{2}D^2 + \frac{3}{8}D^4 - \frac{5}{16}D^6\right)\mathrm{d}\boldsymbol{X}'\right\} \tag{B.16}
$$

The integration terms are insignificant thus can be neglected when the wave steepness is small but will be included in the calculation automatically when wave steepness becomes sufficiently large. More details about the derivation of the formulations can be found in Wang et al. (2018).

References

Adcock, T.A., Taylor, P.H., Draper, S., 2015. Nonlinear dynamics of wave-groups in random seas: unexpected walls of water in the open ocean. Proceedings of the Royal Society A: Mathematical, Physical and Engineering Sciences 471, 20150660.

Adcock, T.A.A., Taylor, P.H., 2014. The physics of anomalous ('rogue') ocean waves. Reports on Progress in Physics 77, 105901.

Alkhalidi, M.A., Tayfun, M.A., 2013. Generalized boccotti distribution for nonlinear wave heights. Ocean engineering 74, 101–106.

Arena, F., Romolo, A., et al., 2005. Random forces on a slender vertical cylinder given by high sea waves interacting with a current. International Journal of Offshore and Polar Engineering 15.

Bakhanov, V.V., Kemarskaya, O., Pozdnyakova, V.P., Okomel'kova, I.A., Shereshevsky, L.A., 1996. Evolution of surface waves of finite amplitude in field of inhomogeneous current, International Geoscience and Remote Sensing Symposium. pp. 609–611.

Baschek, B., Imai, J., 2011. Rogue wave observations off the us west coast. Oceanography 24, 158–165.

Bateman, W.J.D., Swan, C., Taylor, P.H., 2001. On the efficient numerical simulation of directionally spread surface water waves. Journal of Computational Physics 174, 277–305.

Benetazzo, A., Ardhuin, F., Bergamasco, F., Cavaleri, L., Guimaraes, P.V., Schwendeman, M., Sclavo, M., Thomson, J., Torsello, A., 2017. On the shape and likelihood of oceanic rogue waves. Scientific Reports 7, 8276.

Boccotti, P., 1983. Some new results on statistical properties of wind waves. Applied Ocean Research 5, 134–140.

Boccotti, P., 1989. Quasi-determinism of sea wave groups. Meccanica 24, 3–14.

Boccotti, P., 2000. Wave mechanics for ocean engineering. Elsevier.

Boccotti, P., Barbaro, G., Mannino, L., 1993. A field experiment on the mechanics of irregular gravity waves. Journal of Fluid Mechanics 252, 173–186.

Cattrell, A.D., Srokosz, M., Moat, B.I., Marsh, R., 2018. Can rogue waves be predicted using characteristic wave parameters? Journal of Geophysical Research: Oceans 123, 1–13.

Choi, W., 2009. Nonlinear surface waves interacting with a linear shear current. Mathematics and Computers in Simulation 80, 29–36.

Christou, M., Ewans, K., 2014. Field measurements of rogue water waves. Journal of Physical Oceanography 44, 2317–2335.

Clamond, D., Fructus, D., Grue, J., Kristiansen, Ø., 2005. An efficient model for three-dimensional surface wave simulations. part ii: Generation and absorption. Journal of computational physics 205, 686–705.

Dalzell, J., 1999. A note on finite depth second-order wave–wave interactions. Applied Ocean Research 21, 105–111.

Dean, R.G., Sharma, J.N., 1981. Simulation of wave systems due to nonlinear directional spectra, in: International symposium on hydrodynamics in coastal engineering, pp. 1211–22.

Dysthe, K., Krogstad, H.E., Müller, P., 2008. Oceanic rogue waves. Annu. Rev. Fluid Mech. 40, 287–310.

Dysthe, K., Trulsen, K., Krogstad, H.E., Socquet-Juglard, H., 2003. Evolution of a narrow-band spectrum of random surface gravity waves. Journal of Fluid Mechanics 478, 1–10.

El Koussaifi, R., Tikan, A., Toffoli, A., Randoux, S., Suret, P., Onorato, M., 2018. Spontaneous emergence of rogue waves in partially coherent waves: A quantitative experimental comparison between hydrodynamics and optics. Physical Review E 97, 012208.

Ellingsen, S.Å., Li, Y., 2017. Approximate dispersion relations for waves on arbitrary shear flows. Journal of Geophysical Research: Oceans 122, 9889–9905.

Fadaeiazar, E., Alberello, A., Onorato, M., Leontini, J., Frascoli, F., Waseda, T., Toffoli, A., 2018. Wave turbulence and intermittency in directional wave fields. Wave motion 83, 94–101.

Fadaeiazar, E., Leontini, J., Onorato, M., Waseda, T., Alberello, A., Toffoli, A., 2020. Fourier amplitude distribution and intermittency in mechanically generated surface waves. arXiv preprint arXiv:2003.08666 .

Fang, W., Guo, Z., Huang, Y., 1998. Observational study of the circulation in the southern south china sea. Chinese Science Bulletin 43, 898–905.

Fedele, F., 2015. On the kurtosis of deep-water gravity waves. Journal of Fluid Mechanics 782, 25–36.

Fedele, F., Brennan, J., De León, S.P., Dudley, J., Dias, F., 2016. Real world ocean rogue waves explained without the modulational instability. Scientific reports 6, 27715.

Fedele, F., Lugni, C., Chawla, A., 2017. The sinking of the el faro: predicting real world rogue waves during hurricane joaquin. Scientific reports 7, 1–15.

Fedele, F., Tayfun, M.A., 2009. On nonlinear wave groups and crest statistics. Journal of Fluid Mechanics 620, 221.

Forristall, G.Z., 2000. Wave crest distributions: Observations and second-order theory. Journal of physical oceanography 30, 1931–1943.

Gibbs, R.H., Taylor, P.H., 2005. Formation of walls of water in 'fully'nonlinear simulations. Applied Ocean Research 27, 142–157.

Goda, Y., 1983. Analysis of wave grouping and spectra of long-travelled swell. Report of Port and Harbour Research Institute 22, 3–41.

Guyenne, P., 2017. A high-order spectral method for nonlinear water waves in the presence of a linear shear current. Computers & Fluids 154, 224–235.

Hjelmervik, K.B., Trulsen, K., 2009. Freak wave statistics on collinear currents. Journal of Fluid Mechanics 637, 267–284.

Huang, N.E., Chen, D.T., Tung, C.C., Smith, J.R., 1972. Interactions between steady non-uniform currents and gravity waves with applications for current measurements. Journal of Physical Oceanography 2, 420–431.

Hwang, P.A., Wang, D.W., Walsh, E.J., Krabill, W.B., Swift, R.N., 2000. Airborne measurements of the wavenumber spectra of ocean surface waves. part ii: Directional distribution. Journal of Physical Oceanography 30, 2768–2787.

Janssen, P.A., Janssen, A.J., 2019. Asymptotics for the long-time evolution of kurtosis of narrow-band ocean waves. Journal of Fluid Mechanics 859, 790–818.

Janssen, P.A.E.M., 2003. Nonlinear four-wave interactions and freak waves. Journal of Physical Oceanography 33, 863–884.

Janssen, P.A.E.M., 2009. On some consequences of the canonical transformation in the hamiltonian theory of water waves. Journal of Fluid Mechanics 637, 1–44.

Janssen, P.A.E.M., Bidlot, J.R., 2009. On the extension of the freak wave warning system and its verification. European Centre for Medium-Range Weather Forecasts.

Janssen, T.T., Herbers, T.H.C., 2009. Nonlinear wave statistics in a focal zone. Journal of Physical Oceanography 39, 1948–1964.

Jensen, J.J., 2005. Conditional second-order short-crested water waves applied to extreme wave episodes. Journal of Fluid Mechanics 545, 29.

Jonathan, P., Taylor, P.H., 1997. On irregular, nonlinear waves in a spread sea. Transactions-American Society of Mechanical Engineers Journal of Offshore Mechanics and Arctic Engineering 119, 37–41.

Kharif, C., Abid, M., Touboul, J., 2017. Rogue waves in shallow water in the presence of a vertically sheared current. Journal of Ocean Engineering and Marine Energy 3, 301–308.

Kharif, C., Pelinovsky, E., Slunyaev, A., 2009. Rogue Waves in the Ocean. Springer-Verlag.

Lavrenov, I., 2003. Wind-Waves in Oceans: Dynamics and Numerical Simulations. Springer-Verlag Berlin Heidelberg.

Lavrenov, I.V., 1998. The wave energy concentration at the agulhas current off south africa. Natural hazards 17, 117–127.

Lavrenov, I.V., Porubov, A.V., 2006. Three reasons for freak wave generation in the non-uniform current. European Journal of Mechanics-B/Fluids 25, 574–585.

Li, J., Chen, Y., Pan, S., 2016. Modelling of extreme wave climate in china seas. Journal of Coastal Research 75, 522–526.

Liao, B., Dong, G., Ma, Y., Gao, J., 2017. Linear-shear-current modified schrödinger equation for gravity waves in finite water depth. Physical Review E 96, 043111.

Lindgren, G., 1970. Some properties of a normal process near a local maximum. The Annals of Mathematical Statistics 41, 1870–1883.

Lindgren, G., 2006. Slepian models for the stochastic shape of individual lagrange sea waves. Advances in applied probability 38, 430–450.

Longuet-Higgins, M.S., 1963. The effect of non-linearities on statistical distributions in the theory of sea waves. Journal of fluid mechanics 17, 459–480.

Longuet-Higgins, M.S., 1980. On the distribution of the heights of sea waves: some effects of nonlinearity and finite band width. Journal of Geophysical Research: Oceans 85, 1519–1523.

Longuet-Higgins, M.S., Stewart, R.W., 1961. The changes in amplitude of short gravity waves on steady non-uniform currents. Journal of Fluid Mechanics 10, 529–549.

Ma, Y., Ma, X., Perlin, M., Dong, G., 2013. Extreme waves generated by modulational instability on adverse currents. Physics of Fluids 25, 114109.

Manolidis, M., Orzech, M., Simeonov, J., 2019. Rogue wave formation in adverse ocean current gradients. Journal of Marine Science and Engineering 7, 26.

McAllister, M.L., 2017. Analysis of laboratory and field measurements of directionally spread nonlinear ocean waves. Ph.D. thesis. University of Edinburgh.

Moreira, R.M., Peregrine, D.H., 2012. Nonlinear interactions between deep-water waves and currents. Journal of Fluid Mechanics 691, 1–25.

Mori, N., Janssen, P.A.E.M., 2006. On kurtosis and occurrence probability of freak waves. Journal of Physical Oceanography 36, 1471–1483.

Nava, V., Arena, F., Romolo, A., 2006. Non-linear random wave groups with a superimposed current, in: International Conference on Offshore Mechanics and Arctic Engineering, pp. 229–237.

Nørgaard, J.Q.H., Andersen, T.L., 2016. Can the rayleigh distribution be used to determine extreme wave heights in non-breaking swell conditions? Coastal Engineering 111, 50–59.

Nwogu, O., 1993. Effect of steady currents on directional wave spectra, Proceedings of the 12th International Conference on Offshore Mechanics and Arctic Engineering.

Nwogu, O.G., 2009. Interaction of finite-amplitude waves with vertically sheared current fields. Journal of fluid mechanics 627, 179–213.

Onorato, M., Cavaleri, L., Fouques, S., Gramstad, O., Janssen, P.A.E.M., Monbaliu, J., Osborne, A.R., Packozdi, C., Serio, M., Stansberg, C.T., et al., 2009. Statistical properties of mechanically generated surface gravity waves: a laboratory experiment in a three-dimensional wave basin. Journal of Fluid Mechanics 627, 235–257.

Onorato, M., Osborne, A.R., Serio, M., 2008. On deviations from gaussian statistics for surface gravity waves, In Proceedings of the Hawaiian Winter Workshop, University of Hawaii.

Onorato, M., Osborne, A.R., Serio, M., Cavaleri, L., Brandini, C., Stansberg, C.T., 2004. Observation of strongly non-gaussian statistics for random sea surface gravity waves in wave flume experiments. Physical Review E 70, 067302.

Onorato, M., Osborne, A.R., Serio, M., Cavaleri, L., Brandini, C., Stansberg, C.T., 2006. Extreme waves, modulational instability and second order theory: wave flume experiments on irregular waves. European Journal of Mechanics-B/Fluids 25, 586–601.

Onorato, M., Osborne, A.R., Serio, M., Resio, D., Pushkarev, A., Zakharov, V.E., Brandini, C., 2002. Freely decaying weak turbulence for sea surface gravity waves. Physical review letters 89, 144501.

Onorato, M., Proment, D., Toffoli, A., 2011. Triggering rogue waves in opposing currents. Physical Review Letter 107.

Pelinovsky, E., Kharif, C., et al., 2008. Extreme ocean waves. Springer.

Peregrine, D.H., 1976. Interaction of water waves and currents. Advances in applied mechanics 16, 9–117.

Ruban, V.P., 2012. On the nonlinear schrödinger equation for waves on a nonuniform current. JETP Letter 95, 486–491.

Skourup, J., Hansen, N., Andreasen, K.K., 1997. Non-gaussian extreme waves in the central north sea. J. Offshore Mech. Arctic Engng. 119, 146–150.

Slunyaev, A., Kokorina, A., 2020. Numerical simulation of the sea surface rogue waves within the framework of the potential euler equations. Izvestiya, Atmospheric and Oceanic Physics 56, 179–190.

Slunyaev, A.V., Sergeeva, A.V., 2012. Stochastic simulation of unidirectional intense waves in deep water applied to rogue waves. JETP Lett. 94, 779–786.

Soares, C.G., Cherneva, Z., Antão, E.M., 2003. Characteristics of abnormal waves in north sea storm sea states. Applied Ocean Research 25, 337–344.

Socquet-Juglard, H., Dysthe, K., Trulsen, K., Krogstad, H.E., Liu, J., 2005. Probability distributions of surface gravity waves during spectral changes. Journal of Fluid Mechanics 542, 195–216.

Stocker, J.R., Peregrine, D.H., 1999. The current-modified nonlinear schrödinger equation. Journal of Fluid Mechanics 399, 335–353.

Tang, T., Tromans, P.S., Adcock, T.A., 2019. Field measurement of nonlinear changes to large gravity wave groups. Journal of Fluid Mechanics 873, 1158–1178.

Tayfun, M.A., 1980. Narrow-band nonlinear sea waves. Journal of Geophysical Research: Oceans 85, 1548–1552.

Tayfun, M.A., Fedele, F., 2007a. Expected shape of extreme waves in storm seas, in: International Conference on Offshore Mechanics and Arctic Engineering, pp. 53–60.

Tayfun, M.A., Fedele, F., 2007b. Wave-height distributions and nonlinear effects. Ocean engineering 34, 1631–1649.

Tayfun, M.A., Lo, J.M., 1990. Nonlinear effects on wave envelope and phase. Journal of waterway, port, coastal, and ocean engineering 116, 79–100.

Thomas, R., Kharif, C., Manna, M., 2012. A nonlinear schrödinger equation for water waves on finite depth with constant vorticity. Physics of fluids 24, 127102.

Toffoli, A., Cavaleri, L., Babanin, A.V., Benoit, M., Bitner-Gregersen, E.M., Monbaliu, J., Onorato, M., Osborne, A.R., Stansberg, C.T., et al., 2011. Occurrence of extreme waves in three-dimensional mechanically generated wave fields propagating over an oblique current. Natural Hazards and Earth System Sciences 11, 895–903.

Toffoli, A., Gramstad, O., Trulsen, K., Monbaliu, J., Bitner-Gregersen, E., Onorato, M., 2010. Evolution of weakly nonlinear random directional waves: laboratory experiments and numerical simulations. Journal of Fluid Mechanics 664, 313–336.

Toffoli, A., Lefevre, J., Bitner-Gregersen, E., Monbaliu, J., 2005. Towards the identification of warning criteria: analysis of a ship accident database. Applied Ocean Research 27, 281–291.

Toffoli, A., Waseda, T., Houtani, H., Cavaleri, L., Greaves, D.M., Onorato, M., 2015. Rogue waves in opposing currents: an experimental study on deterministic and stochastic wave trains. Journal of Fluid Mechanics 769, 277–297.

Toffoli, A., Waseda, T., Houtani, H., Kinoshita, T., Collins, K., Proment, D., Onorato, M., 2013. Excitation of rogue waves in a variable medium: An experimental study on the interaction of water waves and currents. Physical Review E 87, 051201.

Touboul, J., Kharif, C., 2016. Effect of vorticity on the generation of rogue waves due to dispersive focusing. Natural Hazards 84, 585–598.

Tromans, P.S., Anaturk, A.R., Hagemeijer, P., 1991. A new model for the kinematics of large ocean waves-application as a design wave, The First International Offshore and Polar Engineering Conference.

Tucker, M., Challenor, P.G., Carter, D., 1984. Numerical simulation of a random sea: a common error and its effect upon wave group statistics. Applied ocean research 6, 118–122.

Tucker, M.J., Pitt, E.G., 2001. Waves in ocean engineering. Volume 5.

Walker, D., Taylor, P.H., Eatock-Taylor, R., 2004. The shape of large surface waves on the open sea and the draupner new year wave. Applied Ocean Research 26, 73–83.

Wang, J., Ma, Q.W., 2015. Numerical techniques on improving computational efficiency of spectral boundary integral method. International Journal for Numerical Methods in Engineering 102, 1638–1669.

Wang, J., Ma, Q.W., Yan, S., 2017. On quantitative errors of two simplified unsteady models for simulating unidirectional nonlinear random waves on large scale in deep sea. Physics of Fluids 29, 067107.

Wang, J., Ma, Q.W., Yan, S., 2018. A fully nonlinear numerical method for modeling wave–current interactions. Journal of Computational Physics 369, 173–190.

Waseda, T., Kinoshita, T., Tamura, H., 2009. Evolution of a random directional wave and freak wave occurrence. Journal of Physical Oceanography 39, 621–639.

White, B.S., Fornberg, B., 1998. On the chance of freak waves at sea. Journal of fluid mechanics 355, 113–138.

Whittaker, C.N., Raby, A.C., Fitzgerald, C.J., Taylor, P.H., 2016. The average shape of large waves in the coastal zone. Coastal Engineering 114, 253–264.

Wu, C.H., Yao, A., 2004. Laboratory measurements of limiting freak waves on currents. Journal of Geophysical Research: Oceans 109, C12002.

Xiao, W., Liu, Y., Wu, G., Yue, D.K.P., 2013. Rogue wave occurrence and dynamics by direct simulations of nonlinear wave-field evolution. Journal of Fluid Mechanics 720, 357–392.

Yang, Z.T., Liu, P.L.F., 2020. Depth-integrated wave–current models. part 1. two-dimensional formulation and applications. Journal of Fluid Mechanics 883.

Zhang, H.D., Soares, C.G., Chalikov, D., Toffoli, A., 2016. Modeling the spatial evolutions of nonlinear unidirectional surface gravity waves with fully nonlinear numerical method. Ocean Engineering 125, 60–69.